A non local model for cell migration in response to mechanical stimuli

Original
A non local model for cell migration in response to mechanical stimuli / Marchello, Roberto; Colombi, Annachiara; Preziosi, Luigi; Giverso, Chiara. - In: MATHEMATICAL BIOSCIENCES. - ISSN 0025-5564. - 368:(2024), pp. 1-22. [10.1016/j.mbs.2023.109124]

Publisher:
Elsevier

Published
DOI:10.1016/j.mbs.2023.109124

Mathematical Biosciences 368 (2024) 109124

Contents lists available at ScienceDirect

Mathematical Biosciences

journal homepage: www.elsevier.com/locate/mbs

Original Research Article

A non local model for cell migration in response to mechanical stimuli

Roberto Marchello [a], Annachiara Colombi [b], Luigi Preziosi [b], Chiara Giverso [b],*

[a] Mathematics Area, SISSA (International School for Advanced Studies), Via Bonomea 265, Trieste, 34136, Italy
[b] Department of Mathematical Sciences G. L. Lagrange, Politecnico di Torino, C.so Duca degli Abruzzi 24, Torino, 10129, Italy

ARTICLE INFO

MSC:
92C17

Keywords:
Cell migration
Durotaxis
Tensotaxis
Substrate deformation
Non-local integro-differential model

ABSTRACT

Cell migration is one of the most studied phenomena in biology since it plays a fundamental role in many physiological and pathological processes such as morphogenesis, wound healing and tumorigenesis. In recent years, researchers have performed experiments showing that cells can migrate in response to mechanical stimuli of the substrate they adhere to. Motion towards regions of the substrate with higher stiffness is called *durotaxis*, while motion guided by the stress or the deformation of the substrate itself is called *tensotaxis*. Unlike chemotaxis (i.e. the motion in response to a chemical stimulus), these migratory processes are not yet fully understood from a biological point of view. In this respect, we present a mathematical model of single-cell migration in response to mechanical stimuli, in order to simulate these two processes. Specifically, the cell moves by changing its direction of polarization and its motility according to material properties of the substrate (e.g., stiffness) or in response to proper scalar measures of the substrate strain or stress. The equations of motion of the cell are non-local integro-differential equations, with the addition of a stochastic term to account for random Brownian motion. The mechanical stimulus to be integrated in the equations of motion is defined according to experimental measurements found in literature, in the case of durotaxis. Conversely, in the case of tensotaxis, substrate strain and stress are given by the solution of the mechanical problem, assuming that the extracellular matrix behaves as a hyperelastic Yeoh's solid. In both cases, the proposed model is validated through numerical simulations that qualitatively reproduce different experimental scenarios.

1. Introduction

Cell migration is a critical phenomenon occurring in several biological processes, such as morphogenesis, wound healing and tumorigenesis [1,2]. Specifically, cell motility deficiency is associated with the occurrence of anomalies and complications [3,4], such as neuronal development disorders, immunodeficiency, and neurodegenerative diseases, that can compromise short-term or long-term health of individuals. Understanding cell migration as an integrated and coordinated process, considering both the stimuli and mechanisms involved, may help in the development of new therapeutic approaches to fight pathological processes [5].

The initiation of the whole process of cell migration requires the polarization of the cell in order to discriminate the leading edge from the trailing edge and implies a loss of symmetry from the stationary configuration [6–10]. Cell polarization can be either self-regulated, leading to either an unbiased or a persistent random walk in the absence of external signals [11], or triggered by various stimuli, including diffusible chemical cues (chemotaxis [12,13]), substrate-bound chemicals or cellular adhesion sites (haptotaxis [12,14]), mechanical substrate compliance (durotaxis [15–19]), mechanical deformation of the substrate (tensotaxis [15,20]), geometric features of the substrate (topotaxis [12,21]), electric fields (galvanotaxis [12,22]), light intensity gradients (phototaxis [23,24]), fluid flows (rheotaxis [25,26]), acoustic waves (acoustotaxis [27]). The external stimulus is converted into internal gradients of signaling molecules that guide the cytoskeleton mechanisms performing the motile response [9,28,29].

For the purpose of this work, we will focus on cell movement driven by mechanical stimuli, i.e. durotaxis and tensotaxis. One of the first experimental studies in this respect was developed by Lo et al. [15] who evaluated the influence of the stiffness gradient on cellular locomotion, and introduced the term durotaxis to denote this rigidity-guided cell movement. In their experiments, performed on a collagen-coated polyacrylamide substrate sheet, half soft and half stiff, fibroblasts either migrated onto the stiffest side when they are initially placed on the soft side, or stayed on the stiffest side when they are seeded there. These results showed that fibroblasts are able to implement an active tactile exploration of their environment and that they prefer stiffer matrices to softer ones. Similar results have been obtained more recently in [30] using pancreatic cells. The molecular mechanisms regulating such cellular response to the stiffness of the

---

* Corresponding author.
E-mail address: chiara.giverso@polito.it (C. Giverso).

https://doi.org/10.1016/j.mbs.2023.109124
Received 7 April 2023; Received in revised form 17 November 2023; Accepted 5 December 2023

Table 1
Summary table with the models for cell migration due to mechanical stimuli reviewed in Section 1.

Model	Processes	Dim.	Ref.
Continuum	Durotaxis, tensotaxis	2D	[20]
Continuum	Tensotaxis	2D	[5]
Continuum	Tensotaxis	2D	[41]
CPM	Durotaxis	2D	[42]
Hybrid CPM and FEM extended with ODE–based models for FA turnover	Durotaxis, FA evolution	2D	[16]
IBM	Durotaxis, cell–matrix interaction	2D	[43]
Discrete	Durotaxis	2D	[44]
Hybrid discrete–continuum	Tensotaxis	2D	[40]
Level set method	Durotaxis, tensotaxis, cell shape evolution	2D	[35]
Stochastic Fokker–Planck equation	Durotaxis	1D	[45]
Stochastic Fokker–Planck equation	Durotaxis	2D	[46]
Tensegrity	Durotaxis, tensotaxis	1D, 3D	[47]
Continuum model of fluid–structure interaction	Tensotaxis	2D, 3D	[37]

extracellular matrix (ECM) are still not completely understood [12,31]. However, a key role is surely played by integrins and focal adhesions (FAs), which are protein complex consisting of clustered integrins and other cytoplasmic molecules connecting the F-actin cytoskeleton with the ECM. At these adhesion sites, integrins transduce mechanical forces generated by the actin retrograde flow and myosin II to the ECM. They also recruit cytoplasmic proteins and activate a mechanism that leads to the alteration of the functions of mechanosensitive proteins within adhesions to elicit biochemical signals that regulate both rapid and long-term responses in cellular mechanics (*mechanotransduction*) [32,33]. Integrins dynamically assemble and disassemble, at a rate that is regulated biochemically and mechanically: the disassembly rate is higher on soft ECMs and is lower on stiffer ECMs, so that FAs stabilize more easily on stiffer ECMs [16].

For what concerns tensotaxis, it has been shown that cells tend to move towards tensile stresses and away from compressive stresses [5,15,20,34–40]. One of the first experimental evidence of this behavior can be found in [38]. Using clusters of epidermal cells artificially extended with a micromanipulated needle, the authors observed that protrusive activity perpendicular to the axis of tension was dramatically suppressed, while cytoskeletal microfilaments aligned themselves parallel to the tension. Further insights were provided by Belussov et al. [36]: evaluating the behavior of the cells in a ventral ectodermic explant under stress, they observed that cells moved to more strained regions of the substrate. Moreover, Lo et al. [15], manipulating a substrate with a microneedle, observed that cells migrate towards the needle when the substrate is pulled away from the cell (tensile stress), and conversely the cell move away from the needle when the substrate is pushed towards the cell (compressive stress). In this respect, even though the mechanotransduction mechanism is not understood yet, it has been proposed that the process of mechanosensing could be mediated by the deformation energy associated with the substrate, rather than stresses and stiffness. In fact, in [34], the authors seeded cells on substrates of the same stiffness with different levels of pre-strain, finding out that cell are able to recognize the presence of a pre-strain, exhibiting a stiffer cytoskeleton on stretched material than on unstretched substrate.

The study of cell migration in response to external stimuli has gained attention also from the mathematical and physical communities. However, the theoretical and computational modeling approaches proposed in literature to describe cell motion guided by external cues mainly regard the process of chemotaxis, while only recently some mathematical models have been proposed to describe durotaxis and tensotaxis.

Focusing the attention on the mathematical description of cell motion driven by mechanical stimuli, one of the first continuum mechanobiological models was developed by Moreo et al. [20] to study the adherent cell migration onto a 2D environment. In this work, the cell–ECM interaction was characterized as an elastic spring system, representing the main components of the cell (microtubules of the cytoskeleton, actin bundles and the actomyosin machinery) and the matrix. In [5], the previous model was generalized to study the migration of adherent cells inside a porous medium, considering the influence of the extracellular matrix and of the interstitial fluid on the behavior of cells. Another continuum model is developed in [41], where the authors show that cells moving on predeformed thin elastic membrane follow the direction of increasing strain of the substrate. In [16,42], a Cellular Potts Model (CPM) was used to simulate single cell migration over flat substrates with variable stiffness and the numerical results showed a good qualitative agreement with experimental observations. However, a quantitative validation of the proposed model would be impossible, since some of the parameters cannot be associated directly with physically known quantities.

Agent (or individual) based models have been largely used to model cell migration driven by mechanical stimuli, as well. Specifically, in [43] the authors proposed a force-based individual-based modeling framework that links single-cell migration with matrix fibers and cell–matrix interactions, highlighting the effect of the cell's environment on its migration. A similar model, proposed in [44], consists of a cell, represented by a polarization vector and a sensing region, generating contractile forces on a deformable substrate coarse-grained into an irregular triangulated mesh. A hybrid discrete-continuum description of cells migrating on a deformed substrate using an agent-based model has been proposed also in [40], where the cell moving probabilities are influenced by deformations within the substrate and cells preferentially follow the direction of highest strain. On the other hand, a very different mathematical technique has been used in [35], where the authors employed a level set method to study keratocyte cell shape evolution depending on the substrate stress either generated by the cells themselves or externally applied. Lastly, regarding other modeling approaches, stochastic models exploiting the Fokker–Planck equation [45,46], tensegrity models [47], and multiphysics phase-field model of fluid–solid interaction [37] have been proposed. In Table 1 we gather the models for cell migration in response to mechanical stimuli reviewed in this section.

Bearing in mind the above mentioned biological and mathematical works on cell motion and drawing inspiration from the model presented by Colombi et al. [48] for cell motion in response to chemotaxic cues and ECM density, in this work we present a new non-local integro-differential mathematical model for the migration of a single-cell onto a bidimensional substrate in response to mechanical cues, to reproduce the phenomena of durotaxis and tensotaxis. In its core the model describes a Brownian motion of a point particle in a two dimensional space, with a sensing region which is a circle of the dimension of the protruding cell. The framework is then specialized to phenomenologically and qualitatively describe the motion of the cell during durotaxis

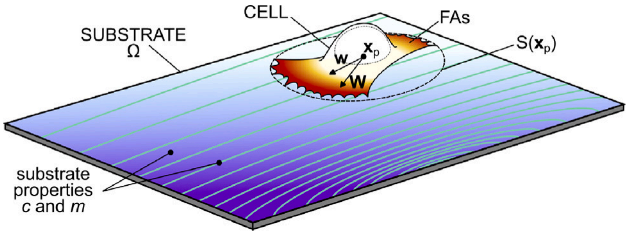

Fig. 1. System representation. The upper face of the substrate is represented by an open and connected set Ω. The cell is described as a point-wise particle located at $\mathbf{x}_p(t) \in \Omega$. The vector $\mathbf{w}$ denotes the present direction of polarization of the cell while $\mathbf{W}$ is the preferred direction of polarization dictated by the environmental mechanical stimuli c and m sensed by the cell within the sensing region $\mathcal{S}(\mathbf{x}_p)$ through its focal adhesion (FAs).

and tensotaxis. In the former case, we will deal with different patterns of substrate stiffness inspired by the experimental literature. In the latter, substrate deformation (and relative strain/stress) will be computed numerically by assuming that the material behaves as a hyperelastic Yeoh's solid, as tested experimentally [49], and the in-silico cell will migrate in response to proper scalar measures of the substrate mechanical response. It is important to clarify that we will not model the subcellular mechanisms involved in the migration, but we will give a purely phenomenological description of their effect at the cellular scale. Therefore, durotaxis and tensotaxis will be treated separately, within the same mathematical framework, even though they likely involve similar subcellular mechanisms, i.e. the mechanotransduction process in response to either substrate stiffness or substrate strains and stresses could activate the same intracellular pathways [50–52].

Specifically, in Section 2 we present the mathematical model for cell migration onto a bidimensional matrix, in response to mechanical stimuli, describing first the general structure of the non-local integro-differential mathematical framework (Section 2.1) and then the specific choices of the functional fields involved in the model (Sections 2.2–2.3) that allow us to reproduce qualitatively the behavior of cells during durotaxis and tensotaxis. The existence and uniqueness of the solution of the proposed model, as well as its continuous dependence on the initial condition, is discussed in Appendix A. Then, in Section 3, we give some details on the numerical implementation of the model for cell dynamics and the mechanical problem for substrate deformation. Section 4 is devoted to numerical results showing the potentiality of our model, in the case of both durotaxis (Section 4.1) and tensotaxis (Section 4.2), by considering different scenarios inspired by the experimental literature and model parameters in the biological range (see Appendix B for the comprehensive derivation of the parameters). In Section 5, after a short summary of the main outcomes of our work, we discuss the limitations of the proposed model and possible future developments.

2. Mathematical model

2.1. General mathematical framework for cell dynamics in response to mechanical stimuli

The proposed model is based on an discrete representation of the single cell coupled with a continuous description of the mechanical properties and behavior of the substrate. The planar substrate on which the cell is seeded is modeled as a thin solid with negligible thickness, whose upper face is represented by an open and connected set Ω. Thus, the representative cell is described as a point-wise particle characterized, at any instant of time $t \in \mathbb{R}_0^+$, by the position of its center $\mathbf{x}_p(t) \in \Omega$ (see Fig. 1). The extreme viscosity of biological environments leads inertial effects on cell dynamics to be negligible. Thus the time evolution of cell position can be described through a first-order differential equation, i.e. cell dynamics is assumed proportional to cell velocity rather than to cell acceleration. As recalled in Section 1, in the absence of environmental stimuli or other individuals a cell performs an unbiased Brownian motion exploring the surrounding environment, whereas when the cell detects an external cue, it can direct its movement in response to it. Therefore, the cell overall displacement can be assumed as resulting from the superposition of a random term implementing cell Brownian motion and a directional term triggered, in the case of our interest, by environmental mechanical stimuli. This leads to the following stochastic differential equation for cell dynamics

$$\mathrm{d}\mathbf{x}_p(t) = \sqrt{2D}\,\mathrm{d}\mathbf{B}(t) + v(t)\,\mathbf{w}(t)\,\mathrm{d}t. \tag{1}$$

In the first term in Eq. (1), $\mathbf{B}(t)$ denotes a vector Wiener process [53–55], while D is the diffusion coefficient characterizing cells Brownian motion on ECM at the macroscopic scale. In fact, according to [53,56], the term $\sqrt{2D}$ is a good approximation of the magnitude of cell random motion. The second term in Eq. (1), instead, incorporates the cell *direction of polarization* $\mathbf{w} \in \mathbb{R}^2$ (see again Fig. 1) and the biased cell *motility* $v \in \mathbb{R}^+$, both triggered by the environmental stimuli. Indeed, when the cell senses an environmental cue, it reorganizes and reassembles its internal cytoskeletal structure in order to distinguishing a leading and a rear edge, thus identifying its *direction of polarization*. The cell ability to actually migrate in the direction of polarization, is given by the *cell motility*, which is related to the rate of assembly and disassembly (at the leading and at the rear edge, respectively) of stable FAs that anchor cell cytoskeleton to the ECM, as well as by polymerization/depolymerization of actin and its retrograde flow (see Section 1). In our setting, in agreement with Colombi et al. [48], we explicitly separate the description of the cell direction of polarization and motility to account for situations in which they are dictated by potentially different environmental stimuli. For instance, it has been experimentally observed that cells placed on a substrate undergoing cyclic stretching can reorient themselves without experiencing an overall movement in the direction of reorientation [57]. Furthermore, although in the context of chemotaxis, it has been shown that directional sensing by eukaryotic cells does not necessarily require polarization of receptors and, at the same time, in cells completely immobilized by inhibitors of actin polymerization, there could be an undiminished polarized response [58,59]. In this work, even though cells are able to simultaneously respond to many different cues, we assume, in a first approximation, that v and $\mathbf{w}$ are respectively affected by a single external cue. We hereafter denote by $m : \mathbb{R}_0^+ \times \Omega \rightarrow [0,1]$ the mechanical cue determining the cell motility v, and by $c : \mathbb{R}_0^+ \times \Omega \rightarrow \mathbb{R}$ the one triggering cell reorientation. These fields will be related to the mechanical properties and behaviors of the substrate along with its composition, to represent the proper mechanical cues driving cell durotaxis and tensotaxis (see Sections 2.2 and 2.3, respectively).

For what concerns cell motility v in Eq. (1), following the approach proposed in [48], we define

$$v(t) = V_M\, f(M(t, \mathbf{x}_p(t), \mathbf{w}(t))), \tag{2}$$

where $V_M > 0$ is the maximum cell motility due to mechanosensing processes and related to the maximum rate of renewal of FAs and cytoskeletal reorganization. The function $f : [0,1] \rightarrow [0,1]$, to be specified according to the process we are considering, non locally measures the stimulus m through its mean M, perceived by the cell ahead its center $\mathbf{x}_p$ and along its polarization direction $\mathbf{w}$ at time t, i.e.

$$M(t, \mathbf{x}_p(t), \mathbf{w}(t)) = \frac{1}{R}\int_0^R m\left(t, \mathbf{x}_p(t) + r\,\frac{\mathbf{w}(t)}{\|\mathbf{w}(t)\|}\right)\mathrm{d}r, \tag{3}$$

where $R > 0$ is the cell maximum protrusion length and $\|\cdot\|$ denotes the Euclidean norm in $\mathbb{R}^2$. Eqs. (2)–(3) translate in mathematical term the biological observation that the cell is able to sense the stimulus m non-locally along the direction of polarization, through specific adhesive receptors (e.g. integrins) and proteins (e.g. small Rho GTPases) that are typically located towards the leading edge identified by the polarization vector $\mathbf{w}$ (i.e. ahead the cell center up to the protrusion end, located at a distance R from $\mathbf{x}_p$).

The reorganization of cytoskeletal filaments to identify or modify the leading and rear edges of a cell is not an instantaneous process. Therefore, the cell polarization vector $\mathbf{w}$ evolves in time, to align itself towards the preferred direction of cell migration $\mathbf{W} \in \mathbb{R}^2$ (see Fig. 1), determined by the spatial distribution of the mechanical cue c. In this respect, as proposed in [48], the cell direction of polarization is assumed to evolve according to the following first order equation

$$\frac{\mathrm{d}\mathbf{w}(t)}{\mathrm{d}t} = \frac{1}{\tau}\left(\frac{\mathbf{W}(t, \mathbf{x}_p(t), \mathbf{w}(t))}{\|\mathbf{W}(t, \mathbf{x}_p(t), \mathbf{w}(t))\| + \varepsilon} - \mathbf{w}(t)\right), \tag{4}$$

where τ is the time needed by the cell to re-orient (persistence time) and $\varepsilon > 0$ is a small constant parameter that ensures that the modulus of the forcing term is smaller than one. It can be proved that Eq. (4) ensures that $\|\mathbf{w}(t)\| \leq 1$ for any $t > 0$, if initially $\|\mathbf{w}(t = 0)\| =: w_0 \in (0, 1]$ (see Proposition 1 in [48]).

Accounting that the preferred direction of cell migration $\mathbf{W} \in \mathbb{R}^2$ is determined by cell ability to sense the surrounding environment through proper membrane receptors, we introduce the so-called sensing region $\mathcal{S}(\mathbf{x}_p(t))$ (see Fig. 1) where the cell may detect local environmental properties and mechanical cues, i.e.

$$\mathcal{S}(\mathbf{x}_p(t)) := \{\mathbf{y} \in \Omega \,:\, \|\mathbf{y} - \mathbf{x}_p(t)\| \leq R\}. \tag{5}$$

Even though this region is roughly assumed to be a circle around the cell center with the radius equal to the maximum membrane protrusion R, accordingly to biological observations, we will further consider that the cell actually senses the mechanical properties of the substrate only in correspondence of the membrane receptors connecting the cell to the matrix [32,33,60–63] (as discussed in Section 1). This phenomenological observation can be mathematically translated in the following equation for the cell preferred direction

$$\mathbf{W}(t, \mathbf{x}_p, \mathbf{w}) = \frac{1}{A}\int_{\mathcal{S}(\mathbf{x}_p)} K\left(\|\mathbf{y} - \mathbf{x}_p\|, \frac{\mathbf{y} - \mathbf{x}_p}{\|\mathbf{y} - \mathbf{x}_p\|} \cdot \frac{\mathbf{w}}{\|\mathbf{w}\|}\right) \left(c(t, \mathbf{y}) - c(t, \bar{\mathbf{z}}(\mathbf{x}_p, \mathbf{w}))\right) \frac{\mathbf{y} - \mathbf{x}_p}{\|\mathbf{y} - \mathbf{x}_p\|}\, \mathrm{d}\mathbf{y}. \tag{6}$$

In Eq. (6), $\bar{\mathbf{z}}(\mathbf{x}_p, \mathbf{w}) = \mathbf{x}_p + aR\frac{\mathbf{w}}{\|\mathbf{w}\|}$, with $a \in (-1, 1)$, is a reference location inside the cell used to evaluate the external stimulus incremental changes along the direction of polarization of the cell. The kernel $K : [0, R] \times [-1, 1] \rightarrow [0, 1]$ is a weight function that measures the capacity of the cell to sense the quantity c, and A is a normalization constant defined as

$$A = \int_{\mathcal{S}(\mathbf{x}_p)} K\left(\|\mathbf{y} - \mathbf{x}_p\|, \frac{\mathbf{y} - \mathbf{x}_p}{\|\mathbf{y} - \mathbf{x}_p\|} \cdot \frac{\mathbf{w}}{\|\mathbf{w}\|}\right) \mathrm{d}\mathbf{y}, \tag{7}$$

whose value is independent of both $\mathbf{x}_p$ and $\mathbf{w}$. Notice that, in the present phenomenological model, despite we do not aim to describe the subcellular mechanisms occurring within the sensing region, the weight function K implements the capacity of the cell to perceive a specific external stimulus c in a non-local and anisotropic way, depending on the expression of membrane mechanosensing receptor. Indeed, the first argument of K is the distance from the cell center $\mathbf{x}_p$ (*non-local sensing*), the latter estimates the angle between the vector $(\mathbf{y} - \mathbf{x}_p)$ and the normalized polarization vector $\mathbf{w}$ (*anisotropic sensing*). Assuming the independence of these two variations, we set

$$K(r, u) = K_r(r)\, K_\theta(u), \tag{8}$$

with $K_r : [0, R] \rightarrow [0, 1]$ and $K_\theta : [-1, 1] \rightarrow [0, 1]$. It is worth to notice that the weight functions K_r and K_θ can assume, each of them, the same functional form in modeling either durotaxis or tensotaxis, since they depend on how the cell detects the substrate stimuli though integrins and FAs. For what concerns K_r, according to the biological observation that integrins and FAs primarily assemble and disassemble at the cell protrusions [16], we assume that the local amount of membrane receptors involved in the mechanotransduction process increases with the distance from the cell center. On the other hand, to define the explicit form of K_θ, we account for the biological observations reported in [60–63], which suggest that the amount of receptors is higher towards cell's front than towards its tail and vanishes perpendicularly to the direction of polarization of the cell.

In this respect, among all the possible choices of the explicit forms of the kernels K_r and K_θ, we hereafter set

$$K_r(r) = \begin{cases} r/R & \text{for} \quad r \in [R_0, R], \\ 0 & \text{for} \quad r \in [0, R_0), \end{cases} \tag{9}$$

with $0 \leq R_0 < R$ (see panel A in Fig. 2), and

$$K_\theta(u) = \begin{cases} \dfrac{1}{4}u^3 + \dfrac{3}{4}u^2 & \text{for} \quad |u| \in [\alpha, 1], \\ 0 & \text{otherwise}, \end{cases} \tag{10}$$

with $\alpha \in [0, 1)$ (see panel B in Fig. 2). Specifically, in Eqs. (9) and (10) the parameters R_0 and α identify the portion of the sensing region where cell membrane receptors are located. Such region is shown in the panel C of Fig. 2, where we plot the whole kernel $K = K_r K_\theta$. Notice that, unless $R_0 = 0$ and $\alpha = 0$ (see the red dashed lines in the panels A and B of Fig. 2), K is discontinuous.

Finally, we remark that other kernels could be considered. However, we have observed that the qualitative results are only slightly influenced by the specific functional form, provided that the biological observations on the distribution of transmembrane receptors are taken into account (see Section 1 of the Supplementary Material, where numerical results with different kernels are reported).

2.2. *Durotaxis: definition of the fields c and m, and of the function f*

As outlined in Section 1, cells can sense the rigidity of the substrate they are anchored to and move towards stiffer regions [15]. In this respect, the simplest phenomenological assumption is to consider the field c affecting cell preferred direction of locomotion, see Eq. (6), as the *stiffness* of the underlying material. Therefore we set

$$c(t, \mathbf{x}) \equiv c(\mathbf{x}) = E(\mathbf{x}) \qquad \forall\ t \in \mathbb{R}_0^+ \text{ and } \mathbf{x} \in \Omega, \tag{11}$$

where E is the Young's modulus of the substrate. Eq. (11) entails that the substrate mechanical properties are fixed in time, since in this specific application we are assuming that the cell does not degrade nor produce extracellular material. Furthermore, we observe that in this case the substrate is undeformed, since possible deformations related to cell motion are disregarded.

On the other hand, in accordance with the mathematical model in [48], we assume that the field m determining the cell speed, i.e. Eq. (3), is related to the *local fraction of ECM proteins* (e.g., Arg-Gly-Asp (RGD) attachment sites that bind to the cell RGD receptors [64]; the extracellular matrix proteins collagen and laminin, that are recognized by the collagen receptors and the laminin receptors, respectively) that influences the cycles of cell motility structures (e.g., lamellipodia, filopodia, pseudopodia) [65,66]. In fact, experimental observations in [67] show that cell migration is slowed down by either low or high densities of matrix binding proteins: in the former case, the cell is unable to find sufficient sites to anchor and use for traction; in the latter, the cell results anchored by stable focal adhesions. Intermediate amounts of ECM densities, instead, result in optimal attachment-detachment cycles and maximal cell speed [67]. In this context, the function f in Eq. (2) writes

$$f(M) = 4M\,(1 - M), \tag{12}$$

as in [48], being M given in Eq. (3) (see the panel A in Fig. 3).

As done for the mechanical properties of the substrate, we assume that the local fraction of ECM proteins does not depend on time, i.e. $m(t, \mathbf{x}) \equiv m(\mathbf{x})$.

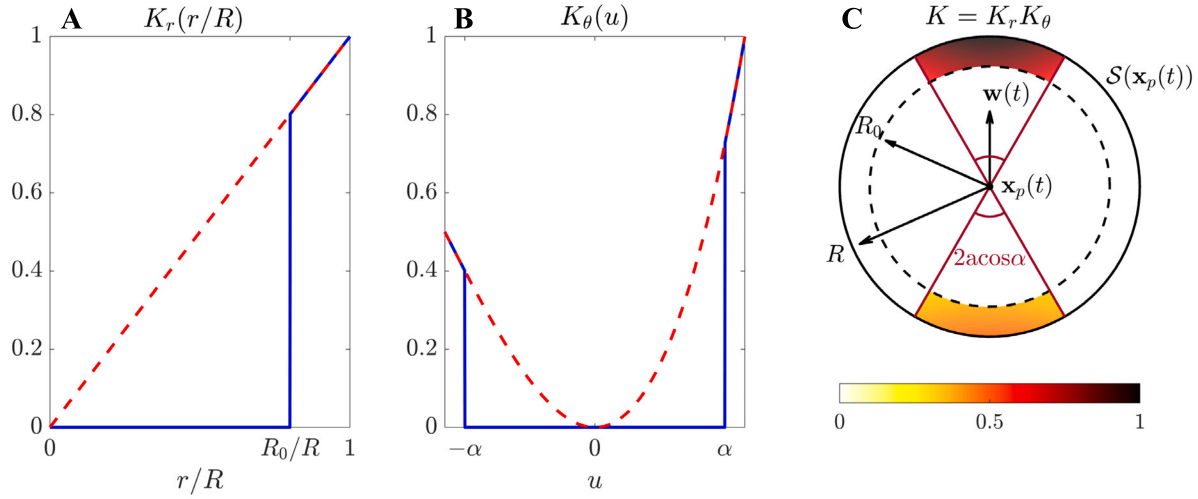

Fig. 2. Different choices of the kernels K_r and K_θ appearing in Eq. (8) for the computation of the cell preferred direction $\mathbf{W}$. (A) Plot of the kernel K_r, defined in Eq. (9), for $R_0 = 0$ (red dashed line) and $R_0 = 4R/5$ (blue line), as set in the numerical simulations. (B) Plot of the kernel K_θ, defined in Eq. (10), for $\alpha = 0$ (red dashed line) and $\alpha = \sqrt{3}/2$ (blue line), as set in the numerical simulations. (C) Plot of the kernel $K = K_r K_\theta$ on the sensing region $\mathcal{S}(\mathbf{x}_p(t))$.

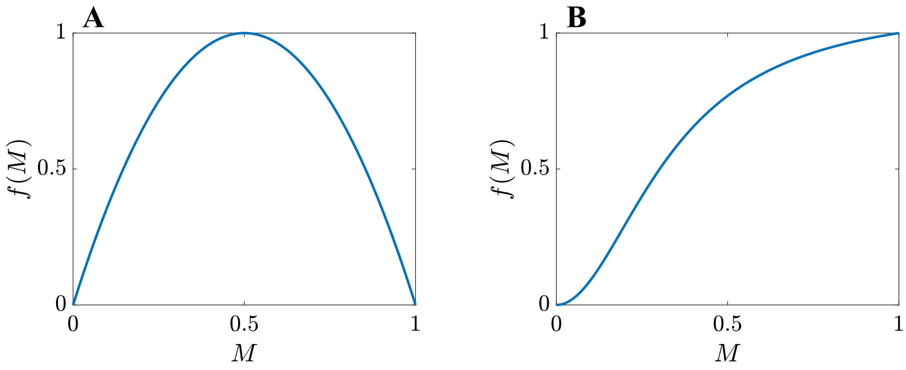

Fig. 3. Representations of function f in Eq. (2). (A) In case of durotaxis, f is assumed as defined in Eq. (12). (B) In case of tensotaxis, f is given by Eq. (20) and here displayed assuming $d = 3$.

2.3. Tensotaxis: definition of the fields c and m, and of the function f

The process of tensotaxis, experimentally observed for instance in [15], consists in cell preference to move towards tensile stresses and away from compressive stresses induced on the substrate. In order to include this qualitative observation in our model, the field c and m, responsible of cell polarization and biased motility, has to be related to proper measures of the substrate mechanical response that allows to take into account the correct direction and speed of the tensotaxis process. Hence, proper balance equations have to be defined in order to describe the mechanical response of the substrate to an external mechanical manipulation and derive the spatio-temporal distributions of the mechanical cues affecting cell migration during tensotaxis.

In this perspective, let $\mathcal{B}_*$ be the reference configuration of the substrate and denote with $\mathbf{X}$ the Lagrangian (or material) coordinates of a material point in this configuration. Then, we identify with $\mathcal{B}_t$ the current configuration of the substrate at time t and we denote with $\mathbf{x}$ the Eulerian (or spatial) coordinates in $\mathcal{B}_t$. According to the standard notation in Continuum Mechanics, we can introduce the displacement field $\mathbf{u}$ and define $\mathbf{x}(t, \mathbf{X}) = \mathbf{X} + \mathbf{u}(t, \mathbf{X})$. Then, the deformation gradient tensor $\mathbb{F}$ is defined as $\mathbb{F} := \mathbb{I} + \text{Grad}\,\mathbf{u}$, being $\text{Grad}(\cdot)$ the gradient with respect to the material coordinates and $\mathbb{I}$ the second order identity tensor.

Recalling that the substrate on which the cell migrates is represented as a thin solid, we can work in the plane stress approximation. Neglecting inertial terms and assuming a static load condition, the balance of linear momentum in Lagrangian coordinates thus reads

$$\frac{\mathbf{b}_s}{h} + \text{Div}\,\mathbb{P} = \mathbf{0}, \quad \text{in } \Omega, \tag{13}$$

where $\mathbf{b}_s$ is the force per unit surface applied on the substrate in the reference configuration, h denotes the thickness of the substrate, $\text{Div}(\cdot)$ is the divergence operator with respect to the material coordinates, and $\mathbb{P}$ is the in-plane first Piola–Kirchhoff stress tensor. Considering a non-linear hyperelastic behavior of the substrate, the first Piola–Kirchhoff stress tensor can be derived from the strain energy density function W:

$$\mathbb{P} = 2\mathbb{F}\,\frac{\partial W}{\partial \mathbb{C}}, \tag{14}$$

being $\mathbb{C} = \mathbb{F}^{\mathsf{T}}\mathbb{F}$ the right Cauchy–Green deformation tensor. The momentum balance Eq. (13) determines the unknown displacement field $\mathbf{u}$, once proper boundary conditions and a functional form for the external surface load $\mathbf{b}_s$ are defined. For the sake of simplicity, we will not include in the model possible stresses or deformations of the substrate generated by the cell itself. Therefore $\mathbf{b}_s$ represents only the external force used to manipulate the substrate. Specifically, in order to reproduce the experimental observations in [15], outlined in Section 1, the pushing or pulling force exerted by the microneedle, localized in a circle $\mathcal{D} \subset \Omega$ sufficiently far from the boundary, is modeled by

$$\mathbf{b}_s = f_b \begin{pmatrix} \cos\beta \\ \sin\beta \end{pmatrix} \mathbb{1}_{\mathcal{D}}, \tag{15}$$

being $\beta \in [0, 2\pi)$ the angle identifying the direction of the imposed load, f_b the magnitude of the force, and $\mathbb{1}_{\mathcal{D}}$ the characteristic function of the subdomain $\mathcal{D}$ where the force of the microneedle is applied. Lastly, since the edges of the substrate in the experiments in [15] are fixed, we prescribe a null displacement at the boundary of the domain, i.e.

$$\mathbf{u} = \mathbf{0} \qquad \text{on} \quad \partial\Omega. \tag{16}$$

We remark that, since we are neglecting the mechanical stress exerted by the moving cell on the substrate Eq. (13) is decoupled from Eqs. (1)–(2). Furthermore, in the case of static deformation we are considering, the displacement and the other derived mechanical fields do not depend on time. Therefore, Eq. (13) can be solved a priori, once and for all, to obtain the spatial evolution of the field c and m fixed in time.

In this perspective, in order to take into account the change of polarization direction experimentally observed in [15] when switching between tensile and compressive stresses, we here assume the field c to be given by the *first invariant of the Cauchy stress tensor*, that is a scalar measure of the mean volumetric stress applied to the deformed substrate, i.e.

$$c(t, \mathbf{x}) \equiv c(\mathbf{x}) = \operatorname{tr} \mathbb{T}(\mathbf{x}) = \operatorname{tr}\left(J^{-1}\mathbb{P}\mathbb{F}^{\top}\right)(\mathbf{x}), \qquad \forall\, t \in \mathbb{R}_0^+ \text{ and } \mathbf{x} \in \Omega, \tag{17}$$

where $J := \det\mathbb{F} > 0$, and $\mathbb{T} = J^{-1}\mathbb{P}\mathbb{F}^{\top}$ defines the Cauchy stress tensor. Thus, according to Eq. (6), a positive value of the field c, corresponding to a volumetric tensile stress, attracts the cell, whereas a negative value, corresponding to a compressive volumetric stress, repels it.

For what concerns the biased cell motility, we take into account the biological observation, mentioned in Section 1, that the mechanosensing process could be also mediated by the elastic energy stored inside the substrate, that promotes a faster cytoskeleton assembly and FA dynamics [34]. We therefore assume that cells move faster over regions with a high elastic energy level, due to the faster breakage of cell–ECM bonds, regardless of whether the substrate is being pulled or pushed. In this respect, the field m in Eq. (3) is here related to the *strain energy density* of the deformed substrate. Following [49], a Yeoh's strain energy density function can well represent the mechanical behavior of the extracellular substrate, thus we set

$$W(\mathbb{C}) = \widehat{W}(I_1, J) = \mu_1(J^{-2/3}I_1 - 3) + \mu_3(J^{-2/3}I_1 - 3)^3 + \frac{2\mu_1(1+\nu)}{3(1-2\nu)}(J-1)^2, \tag{18}$$

where $I_1 = \operatorname{tr}\mathbb{C}$ is the first invariant of the right Cauchy–Green deformation tensor, ν is the substrate Poisson ratio, while μ_1 and μ_3 are material parameters that can be experimentally evaluated and that, in heterogeneous materials, are functions of the material coordinates $\mathbf{X}$. As already done in Section 2.2, we will always assume that substrate mechanical properties are fixed in time, since no mechanism of degradation or deposition of the extracellular material is included in the model. Then, in order to have the field m in the range $[0, 1]$, we consider the following normalization of the energy:

$$m(t, \mathbf{x}) \equiv m(\mathbf{x}) = \frac{W(\mathbf{x})^{1/k_2}}{W(\mathbf{x})^{1/k_2} + \varepsilon_m}, \qquad \forall\, t \in \mathbb{R}_0^+ \text{ and } \mathbf{x} \in \Omega, \tag{19}$$

where the constant parameters k_2 and ε_m are such that $k_2 \geq 1$ and $\varepsilon_m > 0$. Specifically, the exponent $1/k_2$ in Eq. (19) accounts that, for the mechanical force defined in Eq. (15), the energy is extremely localized in the region $\mathcal{D}$ where the load is applied. A proper tuning of this exponent allows the cell to properly sense the field within a distance compatible with the one reported in the biological experiments. In turn, the function f in Eq. (2) has to implement that an increase in the level of the elastic energy, stored in the substrate, sensed by the cell results in an increase of cell speed, promoted by a faster renewal of FA's assembly. With this purpose we define

$$f(M) = \frac{(1+d^2)M^2}{1+(dM)^2}, \tag{20}$$

with $d > 0$ (see panel B in Fig. 3), where M is given in Eq. (3). The normalization in Eq. (20) implements that cell biased motility reaches its maximum value when the amount of energy perceived by the cell reaches the maximum stored energy.

3. Numerical implementation

The cell migration model in Eqs. (1)–(2) is solved on a square domain $\Omega = [0, L] \times [0, L]$ with a finite difference scheme, i.e. the explicit Euler–Maruyama method [68] for both durotaxis and tensotaxis.

The numerical approximation of the integrals M in Eq. (3) and $\mathbf{W}$ in Eq. (6) requires suitable quadrature formulas able to handle possible non-regularities of their integrand functions (given by either the fields m and c, or by the kernels K_r and K_θ). In this perspective, the tailored application of the Gauss–Legendre quadrature formula proposed in [48] is here adapted to deal with the kernels K_r and K_θ in Eqs. (9) and (10) (as well as with those discussed in Section 1 of the Supplementary Material).

In the case of tensotaxis, Eq. (13) is solved with the Finite Element Method (FEM) and an interpolation method is used to evaluate the fields m and c needed to apply the scheme for Eqs. (1)–(2) defined above. The FEM used to solve Eq. (13) was implemented using the *Structural Mechanics Module* of the software *COMSOL Multiphysics*®. A representative case of the unstructured mesh used in the simulations discussed in Section 4.2 is shown in panel (A) of Fig. 4. The grid is characterized by smaller mesh elements at the center of the domain, where the load is applied, in order to properly capture substrate deformation, and relative strain and stress. The mechanical quantities of interest for the cell migration model (i.e. the fields m and c) are then estimated over a $\Lambda \times \Lambda$ square grid with element size $\Delta x = L/\Lambda$ in both directions, as shown in panel (B) of Fig. 4, and then used as an input in the finite difference scheme for cell motion. In this respect, we remark that when tensotaxis is concerned, the fields m and c come from the solution of the momentum balance Eq. (13) in the reference configuration, so the values interpolated over the squared undeformed grid (in panel (b) of Fig. 4) refers to the Lagrangian coordinates system. Cell motion conversely occurs on the deformed substrate, sensing the fields in the current configuration, i.e. $c(\mathbf{x})$ and $m(\mathbf{x})$. Thus, the quantities of interest have to be considered as functions of the Eulerian coordinates. To tackle this issue it is sufficient to apply the computed deformation field $\mathbf{u}$ to the regular grid. Denoting the points of the regular grid by $\mathbf{X}_{ij} \in \Omega$, with $i, j = 1, \dots, \Lambda$, the corresponding deformed ones are identified by

$$\mathbf{x}_{ij} = \mathbf{X}_{ij} + \mathbf{u}(\mathbf{X}_{ij}). \tag{21}$$

Then, the fields m and c are known on the spatial nodes $\mathbf{x}_{ij}$ and are such that

$$m(\mathbf{x}_{ij}) = m(\mathbf{X}_{ij} + \mathbf{u}(\mathbf{X}_{ij})), \qquad c(\mathbf{x}_{ij}) = c(\mathbf{X}_{ij} + \mathbf{u}(\mathbf{X}_{ij})). \tag{22}$$

The points of the deformed grid (see panel (C) of Fig. 4) may not coincide in general with the quadrature nodes needed to evaluate the integral terms in Eqs. (3) and (6). It is then necessary to use a suitable interpolation method to approximate the missing data. Similarly to what was done in [48], through a proper numerical sensitivity analysis, we found that a linear interpolation from this irregular grid to the quadrature nodes and eight nodes of quadrature are enough to preserve the accuracy of the numerical scheme for the computation of the cell trajectory. An analogous analysis allowed us to set the time step $\Delta t = 288$ s and the dimension of the regular grid $\Lambda = 70$. The same time step has been used also in the case of durotaxis.

4. Numerical results

In order to highlight the potential of the proposed model, in this Section, we present several numerical simulations reproducing cell dynamics driven by either durotaxis (see Section 4.1) or tensotaxis (see Section 4.2). In both cases, the fields c and m, and the function f,

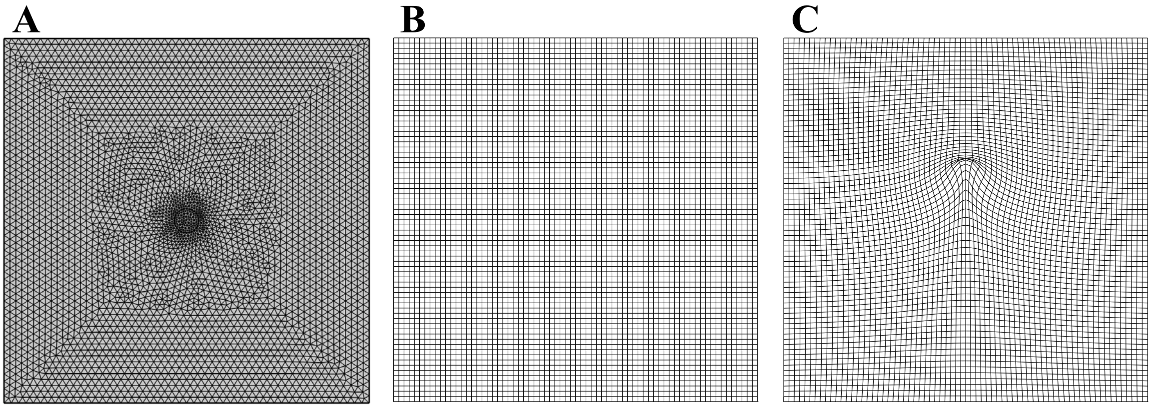

Fig. 4. Panel (A) shows an example of a triangular mesh for the domain Ω automatically generated by the software *COMSOL Multiphysics®* to solve the mechanical problem defined in Section 2. Panel (B) shows an example of a $\Lambda \times \Lambda$ grid with $\Lambda = 70$ used for the extrapolation of the fields m and c to be integrated in the cell motion model. Panel (C) shows the same grid as panel (B) when deformed according to the external manipulation of the substrate, as defined in Eq. (21).

Table 2
Values of the parameters introduced in Section 2 and used in all the numerical simulations, each one with a brief description and references that justify the choices. The top block contains the parameters characterizing cell dynamics, the central and bottom blocks define substrate properties in the case of durotaxis and tensotaxis, respectively.

Par.	Description	Value	Ref.
L	Length of the squared domain Ω	700 μm	[69]
R	Maximum extension of cell protrusions	20 μm	[48,70]
D	Diffusion coefficient of fibroblasts on ECM	1.7×10^{-2} μm²/s	[71–73]
V_M	Cell characteristic speed	0.009 μm/s	[15,48]
τ	Cell re-orientation time	600 s	[15]
R_0	Radial extension of the portion of the sensing region where FAs are located	16 μm	[61,62]
α	$\arccos \alpha$ is the amplitude of the portion of the sensing region where FAs are located	$\sqrt{3}/2$	[61,62]
ε	Michaelis–Menten constant	3.18×10^{-5}	(estimated)
E	Young's modulus	10–100 kPa	[15,74–76]
ν	Poisson ratio of the substrate	0.48	[49]
μ_1	Material elastic coefficient of the substrate (linear)	1.46–4.66 kPa	[49]
μ_3	Material elastic coefficient of the substrate (non-linear)	0.25–5.4 kPa	[49]
h	Substrate thickness	35 μm	[49]

are assumed to depend on the mechanical properties of the substrate according to the phenomenological definitions provided in Sections 2.2 and 2.3, respectively. All the following numerical simulations are performed by setting the values of the model parameter as listed in Table 2, according to the pertinent literature (more details are reported in Appendix B). For each case, we will show, only 10 representative realizations of the cell trajectory. Then, a quantitative analysis of $Q = 50$ different realizations of cell trajectories will be performed by estimating six quantities (defined below): the mean speed $\bar{s}$, the mean motility $\bar{v}$, the overall displacement d^{TOT}, the maximum distance from the initial position $d^{\max}$, the persistence P and the forward migration index FMI.

Denoting by $\mathbf{x}^q_{p,n}$ with $n = 0, 1, \dots, N$ the position of cell center at the time instant t_n in the qth realization, and by $< \cdot >$ the mean over the Q realizations, the *mean speed* $\bar{s}$ is computed as

$$\bar{s} = \left\langle \frac{1}{N} \sum_{n=0}^{N-1} \frac{\|\mathbf{d}^q_n\|}{\Delta t} \right\rangle, \tag{23}$$

where $\mathbf{d}^q_n := \mathbf{x}^q_{p,n+1} - \mathbf{x}^q_{p,n}$, with $n = 0, \dots, N-1$, is the cell displacement at the instant time t_n. The *mean motility* $\bar{v}$ is the motility v defined in Eq. (2) mediated over all the N time iterations and the Q realizations, i.e. denoting by v^q_n the cell motility at the instant time t_n in the qth realization, $\bar{v}$ writes

$$\bar{v} = \left\langle \frac{1}{N} \sum_{n=0}^{N-1} v^q_n \right\rangle. \tag{24}$$

The *overall displacement* of the cell d^{TOT} and the *maximum cell displacement* from the initial position $d^{\max}$ are computed as

$$d^{\mathrm{TOT}} = \left\langle \|\mathbf{x}^q_{p,N} - \mathbf{x}^q_{p,0}\| \right\rangle, \qquad d^{\max} = \left\langle \max_n \|\mathbf{x}^q_{p,n} - \mathbf{x}^q_{p,0}\| \right\rangle. \tag{25}$$

The *persistence* P, according to [19], is the ratio between the total cell displacement (determined by the first and last positions) and the actual path length L^q, mediated over the Q realizations, i.e.

$$\mathrm{P} = \left\langle \frac{\|\mathbf{x}^q_{p,N} - \mathbf{x}^q_{p,0}\|}{L^q} \right\rangle \quad \text{with} \quad L^q := \sum_{n=0}^{N-1} \|\mathbf{d}^q_n\|. \tag{26}$$

The forward migration index FMI is computed as

$$\mathrm{FMI} = \left\langle \frac{1}{L^q} \sum_{n=0}^{N-1} p^q_n \right\rangle, \tag{27}$$

where p^q_n is the projection of the actual direction of motion $\mathbf{d}^q_n$ in the direction the gradient $\nabla c(\mathbf{x}^q_{p,n})$, if $\|\nabla c(\mathbf{x}^q_{p,n})\| > 0$, and it is null otherwise.

Moreover, in more relevant cases, the proposed analysis is enriched by: the distributions of the angle δ^q_n between the actual direction of motion $\mathbf{d}^q_n$ and the x-axis; the distributions of the angle ω^q_n between the direction of polarization $\mathbf{w}^q_n$ and the x-axis; the distributions of the cell motility v^q_n; and two measures already used for instance in [77], i.e. the time-averaged mean square displacement MSD

$$\mathrm{MSD}(k\Delta t) = \left\langle \frac{1}{(N-k+1)} \sum_{n=0}^{N-k} \|\mathbf{x}^q_{p,n+k} - \mathbf{x}^q_{p,n}\|^2 \right\rangle, \quad \text{with} \quad k = 0,\dots,N, \tag{28}$$

and the temporal angular correlation C

$$\mathrm{C}(k\Delta t) = \left\langle \frac{1}{(N-1-k)} \sum_{n=1}^{N-1-k} \cos(\chi^q_{n+k} - \chi^q_n) \right\rangle, \quad \text{with} \quad k = 1,\dots,N-2, \tag{29}$$

where χ^q_n with $n = 1,\dots,N-1$ is the variation of cell direction of motion at the instant time t_n, i.e. the angle between $\mathbf{d}^q_n$ and $\mathbf{d}^q_{n-1}$.

4.1. Numerical results I - durotaxis

In this Section, we present several numerical simulations reproducing cell migratory behavior driven by the process of durotaxis. Specifically, we will first consider smoothed piecewise constant distributions of c and m that implement a high stiffness and an abundance of ECM proteins, respectively, within a vertical stripe in the middle of the domain. This in silico scenario is inspired by the experimental setting used in [15] where the behavior of cells, seeded onto a polyacrylamide sheet coated with collagen, in response to transitions in rigidity was studied by introducing in the central region of the substrate a discontinuity in the concentration of the bis-acrylamide cross-linker. Cells approaching the transition region from the soft side could easily migrate towards the stiffer side; in contrast, cells migrating from the stiff side turned around or retracted as they reached the discontinuity. Double rigidity hydrogels are used also in the durotaxis experiments proposed in [30]. Furthermore, in the mathematical literature, several authors considered a piecewise constant rigidity of the substrate to test their durotactic models [16,42–44]. Then, inspired by biological experiments on durotaxis performed on gel with a stiffness gradient [19,44,66,74,76], we will implement the experimental setup with a substrate with linearly varying stiffness. In this scenario we consider a homogeneous density of ECM binding sites, as reported in the biological tests [74,76,78]. In the Supplementary Material, we also consider the case where the stiffness gradient is coupled to the local amount of ECM, although not confirmed by biological experiments.

Piecewise constant rigidity and stiffness of the substrate. In accordance with the biological setup used in the durotaxis experiments reported in [15,30] and previous mathematical models [16,42–44], we here consider independent piecewise constant distributions for c and m, that respectively implement a higher substrate rigidity and an abundance of ECM proteins within a vertical stripe in the middle of the domain Ω. Specifically, to ensure the regularity of the fields c and m, needed to guarantee the existence and uniqueness of the solution of Eqs. (1)–(2) (see Appendix A), a smoothing of both piecewise constant fields is considered. Specifically, being $\delta \ll d_1 < d_2$, we define the substrate rigidity, that in the durotaxis model corresponds to the field $c(\mathbf{x})$, as

$$c(\mathbf{x}) = E(\mathbf{x}) = \begin{cases} E_1 & \text{if} \quad x \in [d_1+\delta,\, d_2-\delta], \\ E_2 & \text{if} \quad x \in [0,\, d_1-\delta] \cup [d_2+\delta,\, L], \\ S_1(x) & \text{if} \quad x \in (d_1-\delta,\, d_1+\delta), \\ S_2(x) & \text{if} \quad x \in (d_2-\delta,\, d_2+\delta), \end{cases} \tag{30}$$

for any $\mathbf{x} = (x,y)^T \in \Omega$, where S_1 and S_2 are proper third-degree polynomials that guarantee the differentiability of the field c in the whole domain. The central stripe is defined by $d_1 = 300$ μm, $d_2 = 400$ μm and $\delta = 20$ μm. The mechanical parameters in the homogeneous subdomains E_1 and E_2 are assumed equal to 30 kPa and 14 kPa, respectively, as in [15]. The density of ECM proteins is conversely given by

$$m(\mathbf{x}) = \begin{cases} m_1 & \text{if} \quad x \in [d_1+\delta,\, d_2-\delta], \\ m_2 & \text{if} \quad x \in [0,\, d_1-\delta] \cup [d_2+\delta,\, L], \\ S_3(x) & \text{if} \quad x \in (d_1-\delta,\, d_1+\delta), \\ S_4(x) & \text{if} \quad x \in (d_2-\delta,\, d_2+\delta), \end{cases} \tag{31}$$

with $m_1 = 0.75$ and $m_2 = 0.5$, where S_3 and S_4 are proper third-degree polynomials that guarantee the differentiability of m.

The numerical outcomes in Fig. 5 show cell trajectory starting from three different initial positions $\mathbf{x}_{p,0} := (x_{p,0}, y_{p,0})^T$. The results first show that, over the period of observation, if the cell initial position is sufficiently far from the transition zone (see panel A, where the initial position is about 6 sensing radii away from the strip), it remains on the soft part of the substrate with constant stiffness E_2 and performs a random Brownian motion. Instead, if the cell initial position is close enough to the central strip of stiff substrate (about 2 sensing radii away), after an initial random motion, the cell is able to sense the transition zone (characterized by non-uniform stiffness S_1) within its sensitivity region, and it then rapidly moves towards the stiff strip (see panel B). Consistently, the cell remains on the central stiff strip of the substrate, if initially placed there, despite the presence of the stochastic term (see panel C). We observe that in our setting we have included the soft region on the right, that is never reached by the cell, to avoid boundary effects. From a biological point of view, these results show a qualitative agreement with the experimental observations in [15] and with the numerical simulations in [42,44,79]. From a mathematical point of view, these cell behaviors result from the fact that cell preferred direction $\mathbf{W}$ in Eq. (6) depends on the differential increments of the field c in Eq. (11) within cell sensing region, i.e. within a small area around its position. It thus highlights that the integral in Eq. (6) properly models that cell motion is biased only if the cell senses a non-uniform field c within its sensing region, otherwise it performs a random Brownian motion.

In Table 3 we report the values of the mean speed $\bar{s}$, the mean motility $\bar{v}$, the overall displacement d^{TOT}, the maximum distance from the initial position $d^{\max}$, the persistence P and the forward migration index FMI defined in Eqs. (23)–(27), observed for each initial condition. It can be first noticed that the cell mean motility $\bar{v}$ is higher in the first case, when the cell remains in the soft part of the substrate, and it decreases as the cell spends more time over the stiff part of the substrate. This behavior, that derives from the definition of the integral M in Eq. (3) and the function f in Eq. (12), is consistent with the experimental observation that the cell moves faster on the softer side of the substrate as reported in [15]. We note that the value of mean motility predicted by our model is of the same order of magnitude as the mean speed measured experimentally in [15]. However, the differences in the ability of cells to move are less evident when the total speed is considered, and in this case the values reported are higher than the experimental speed reported in [15]. However, this discrepancy can be resolved by tuning the parameters of the model. Moreover, in Table 3, we have that the highest values of the mean speed $\bar{s}$, and thus the displacements d^{TOT} and $d^{\max}$, are reached for $x_{p,0} = 250$ μm (see panel B in Fig. 5). In fact, in this case, the cell senses the transition zone and thus a non-null biased contribution sums to the stochastic term in Eq. (1). Consistently, also the persistence P and the forward migration index FMI assume their higher value in the case with $x_{p,0} = 250$ μm, where the cell reaches the transition zone. However, the very low values assumed by P and FMI (P< 0.15 and FMI< 0.5) indicate, respectively, that the cell mainly moves along a very tortuous path, and with a low correlation with the substrate stiffness, i.e. the field c. In fact, in this scenario, regardless the initial condition, the cell spends most of the time over regions with uniform stiffness performing an unbiased random motion. In particular, notice that in the case with $x_{p,0} = 180$ μm (panel A in Fig. 5), despite the high value of the mean

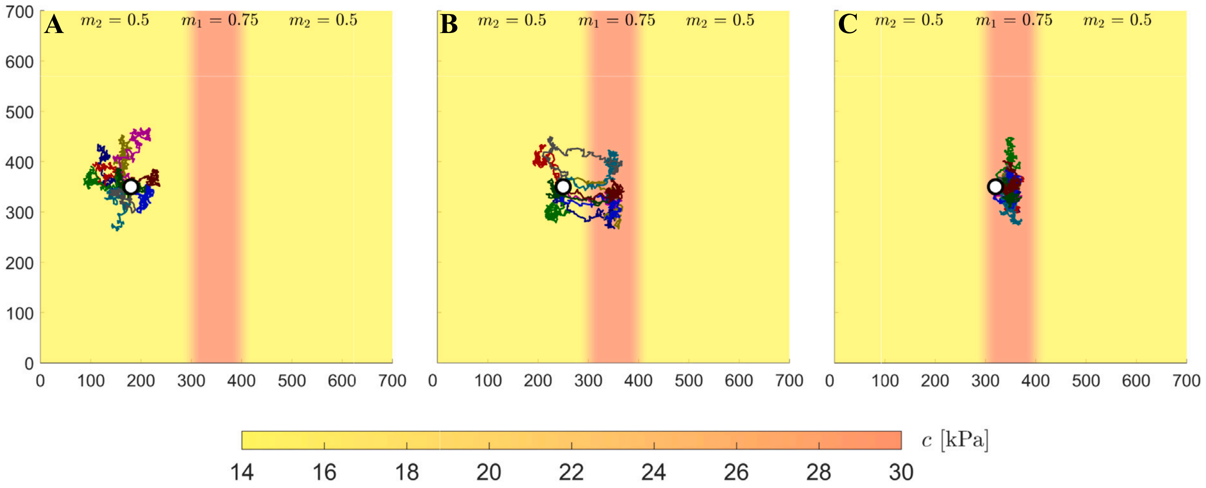

Fig. 5. Numerical simulations reproducing cell dynamics due to durotaxis with piecewise constant fields c and m defined in Eqs. (30) and (31), respectively. Each panel shows 10 different trajectories with the same initial positions, namely (A) $\mathbf{x}_{p,0} = (180, 350)^T$ μm, (B) $\mathbf{x}_{p,0} = (250, 350)^T$ μm, and (C) $\mathbf{x}_{p,0} = (320, 350)^T$ μm (white circles), and with initial polarization $\mathbf{w}_0 = (-1, 0)^T$ (not displayed). We remark that here the initial polarization vector has very little influence on cell behavior: when the cell senses only the homogeneous field, it initially performs a random motion; conversely, close to the central zone with non-uniform stiffness, the cell reorientation is so fast that the trajectory is slightly affected by the initial polarization.

Table 3

Quantitative analysis of the numerical outcomes in Fig. 5, where cell dynamics is driven by durotaxis, and the substrate is characterized by the piecewise constant fields c and m given in Eqs. (30) and (31), respectively. For each panel in Fig. 5, we report the first component of the initial position $x_{p,0}$ (since $y_{p,0} = 350\,\mu$m in all simulations), the mean speed $\bar{s}$ in Eq. (23), the mean motility $\bar{v}$ in Eq. (24), the overall displacement d^{TOT} and the maximum displacement $d^{\max}$ in Eq. (25), the persistence P in Eq. (26) and the forward migration index FMI in Eq. (27).

$x_{p,0}$ [μm]	$\bar{s}$ [μm/s]	$\bar{v}$ [μm/s]	d^{TOT} [μm]	$d^{\max}$ [μm]	P [−]	FMI [−]
180	1.375e−02	9.000e−03	64.24	82.15	0.081	0
250	1.407e−02	7.780e−03	104.79	116.25	0.130	0.041
320	1.387e−02	6.759e−03	44.79	64.97	0.056	0.004

motility, the FMI is null as the cell, remaining always over the softer homogeneous region of the domain, is not affected by the mechanical cue c (i.e. $\mathbf{W} = \mathbf{0}$ in Eq. (6)) and performs an unbiased Brownian motion.

Substrate with linearly varying stiffness and homogeneous ECM density. We here consider a substrate whose stiffness E (corresponding to the c field in our model of durotaxis) smoothly increases in the horizontal direction from the value E_0 to E_L, which are respectively assumed at the left and right end of the domain. According to [44,66,76], we assume the linear field

$$c(\mathbf{x}) = E(\mathbf{x}) = E_0 + \frac{E_L - E_0}{L}\,x. \tag{32}$$

As said at the beginning of this subsection, in accordance with the biological observations reported in [74,76,78], the ECM density m can be defined independently from the stiffness distribution. In this regard, we here consider a homogeneous distribution of the local ECM proteins, i.e.

$$m(\mathbf{x}) = \hat{m}. \tag{33}$$

The numerical results in Fig. 6 show cell trajectories obtained by setting $E_0 = 14$ kPa and $E_L = 30$ kPa in Eq. (32), and by considering different homogeneous ECM density fields $\hat{m}$. Moreover, each panel is provided by polar histograms showing the distributions of the angles ω_n^q and δ_n^q, characterizing the direction of polarization $\mathbf{w}_n^q$ and the actual direction of motion $\mathbf{d}_n^q$, respectively. Dealing with a homogeneous field m, cell motility v is constant in time and thus equal to the mean motility $\bar{v}$ reported in Table 4. In Table 4 we also present the values of the mean speed $\bar{s}$, the overall displacement d^{TOT}, the maximum displacement from the initial position $d^{\max}$, the persistence P and the forward migration index FMI. Lastly, the time evolution of the mean square displacement MSD and the correlation angle C are displayed in Fig. 7.

In contrast to the above striped substrate setup, in this case the motion is always biased towards the right stiffer side of the domain, since the cell always senses a non-uniform substrate stiffness characterized by a constant gradient in the horizontal direction. In this respect, the histograms of ω_n^q in Fig. 6 show that the cell direction of polarization $\mathbf{w}$ is always aligned to the horizontal axis according to the sensed substrate stiffness. However, random effects in cell dynamics introduce discrepancies between the distributions of ω_n^q and δ_n^q, i.e. between the direction of polarization and the actual direction of motion of the cell. In particular, in the case of extremely high/low amount of ECM proteins, there is no a preferred direction of motion indicating that cell dynamics is mainly driven by the random term. Conversely, in other cases the cell mainly move towards the right (stiffer) part of the domain following the field c. Moreover, it emerges that, the overall cell displacement from its initial position changes according to the homogeneous amount of the local fraction of ECM proteins $\hat{m}$. Specifically, the maximum cell displacement is reached when $\hat{m} = 0.5$ (panel C), while either lower or higher values of $\hat{m}$ leads to a reduction of the maximum displacement of the cell. This aspect is even more evident in Table 4 where, in addition, a large/short cell displacement, i.e. high/low d^{TOT} and $d^{\max}$, is always related to high/low mean speed $\bar{s}$, and mean motility $\bar{v}$. In fact, according to the explicit form of f in Eq. (12), in the case of intermediate ECM density, as $\hat{m} = 0.5$, the high cell motility prevails on stochastic contributions in cell velocity leading to a directional motion. This is highlighted by the high values of both P and FMI in Table 4, and the fact that time-averaged MSD in Fig. 7 (panel A) exhibit quadratic growth with time $k\Delta t$, which is typical of drifted motion [77]. Conversely, in the case of low or high ECM density, resulting in low cell motility $\bar{v}$, cell dynamics is mainly dictated by the stochastic contribution and thus resembles a Brownian motion rather than a slower migration towards the right end of the domain (see the cases with $\hat{m} = 0.05$ and $\hat{m} = 0.95$ in panels A and F in Fig. 6). This is confirmed by the relative low values of P and FMI in Table 4, and by the linear growth with time $k\Delta t$ of the time-averaged MSD in Fig. 7 which is typical of simple diffusion. In particular, we observed that, as $\hat{m} \mapsto 0$ or $\hat{m} \mapsto 1$, the time-averaged MSD converges to the straight line $4Dk\Delta t$ (blue solid line in the panel A of Fig. 7) characteristic of the

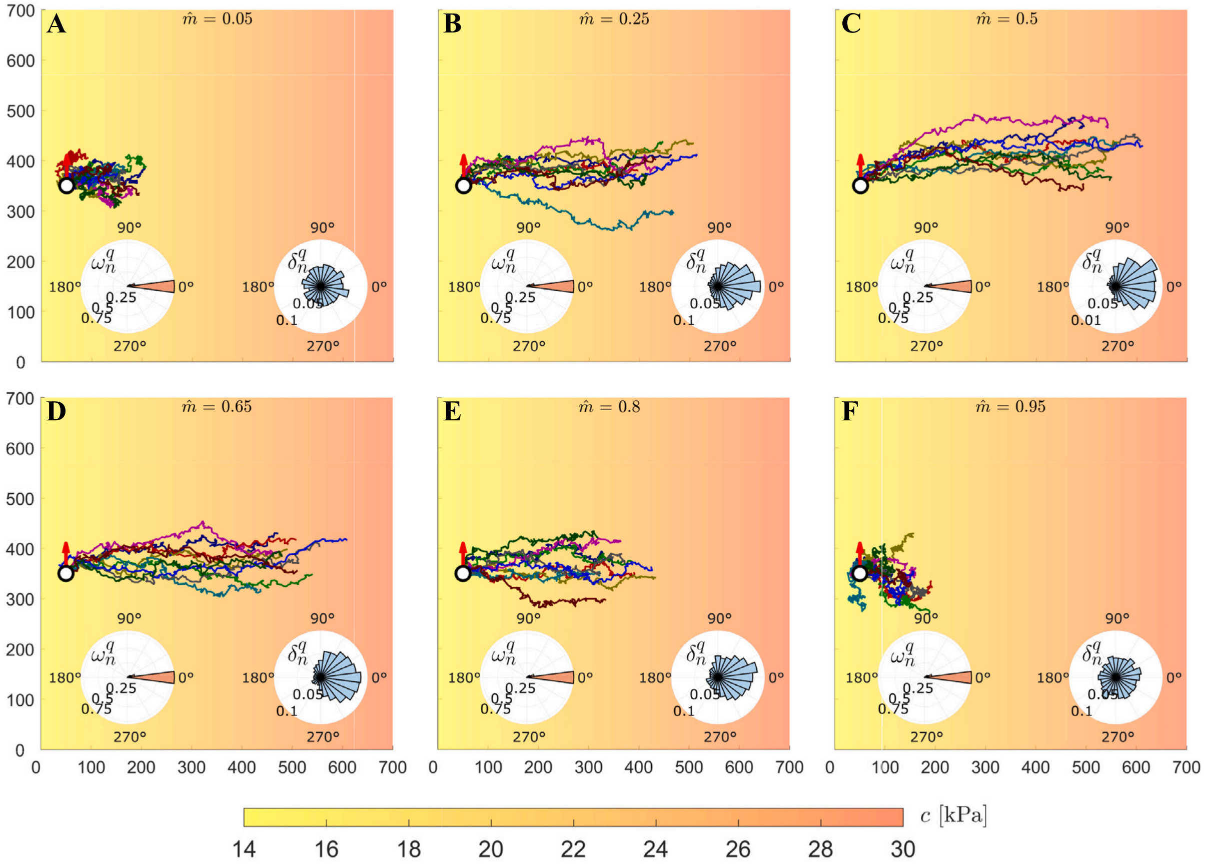

Fig. 6. Numerical simulations reproducing cell dynamics due to durotaxis. The substrate is characterized by the linear field c defined in Eq. (32), and a homogeneous distribution local fraction of ECM proteins m in Eq. (33) with $\hat{m} \in \{0.05, 0.25, 0.5, 0.65, 0.8, 0.95\}$. Each panel shows 10 different trajectories with the same initial conditions, i.e. $\mathbf{x}_{p,0} = (50, 350)^T$ μm (white circle) and $\mathbf{w}_0 = (0, 1)^T$ (red arrow). In each panel, the polar histograms show the distributions of the angles ω_n^q (left) and δ_n^q (right) related to the direction of polarization $\mathbf{w}_n^q$ and the actual direction of motion $\mathbf{d}_n^q$, respectively.

Brownian motion (see [77] for further details). In addition, the plots of the temporal angular correlation in panel B of Fig. 7 highlight that no angular correlation is observed with very low or high values of $\hat{m}$ (having zero average), i.e. there is no connection between the direction of motion at consecutive steps nor at distant steps, confirming that the cell substantially performs a Brownian motion. A low correlation between consecutive directions of motion conversely occurs in the case of intermediate values of $\hat{m}$ (having non-zero average, e.g., ≈ 0.05 when $\hat{m} = 0.5$, see Fig. 7-B). The low values of the angular correlation indicates that, due to the random term, cell trajectory is quite tortuous rather than a straight line along the stiffness gradient.

Interestingly, these results are qualitatively consistent with the experimental observations reported in [74]. Indeed, they found a persistence index for 3T3 cells on gradient gels of around 0.36 ± 0.23, with an average speed of $1.13\text{e} - 02 \pm 0.43\text{e} - 02$ μm/s. Despite the striking agreement between the numerical results and the biological measurements, a quantitative validation of the model using the data in [74] is not possible because the experimental stiffness gradient varies non-linearly between 6 kPa and 60 kPa and the amount of ECM binding proteins (in this case fibronectin) is not reported, although it is said to be approximately homogeneous, as observed in previous works [76,78]

4.2. Numerical results II - tensotaxis

In this section, we then turn to discuss different numerical simulations reproducing cell dynamics when its directional migration is driven by the process of tensotaxis. Biological experiments on tensotaxis are still limited in the literature. Most of them [15,31,36] applied a concentrated force to the substrate by means of a microneedle placed at a distance of 100–200 μm from the cell [31]. The applied force is not reported in the references, but in some cases the displacement of the substrate is recorded [31]. The substrates used to perform the experiments are polyacrylamide gels with homogeneous stiffness in [15,31] and rectangular explants of animal ectoderm extirpated from early gastrula embryos and placed on an adherent agarose substrate in [36], whose mechanical properties, possibly non-homogeneous, are not quantified. Taking inspiration from these biological settings, but without claiming to accurately reproduce any specific experimental tests (due to the lack of more measurements to accurately set the model parameters), we will focus on two different scenarios where the substrate is characterized by either homogeneous or non-homogeneous material parameters μ_1 and μ_3 in Eq. (18), respectively, linked to its linear and non-linear mechanical response to external stimuli.

Table 4
Quantitative analysis of the numerical outcomes in Fig. 6, where cell dynamics is due to durotaxis. The substrate is characterized by the stiffness c in Eq. (32), and by a uniform local fraction of ECM proteins m. For each panel in Fig. 5, we report the value of $\hat{m}$ in Eq. (33), the mean speed $\bar{s}$ in Eq. (23), the mean motility $\bar{v}$ in Eq. (24), the overall displacement d^{TOT} and the maximum displacement $d^{\max}$ in Eq. (25), the persistence P in Eq. (26) and the forward migration index FMI in Eq. (27).

$\hat{m}$	$\bar{s}$ [μm/s]	$\bar{v}$ [μm/s]	d^{TOT} [μm]	$d^{\max}$ [μm]	P [−]	FMI [−]
0.05	1.398e−02	1.710e−03	114.81	121.08	0.143	0.133
0.25	1.493e−02	6.750e−03	397.61	399.29	0.462	0.458
0.5	1.597e−02	9.000e−03	504.03	504.62	0.548	0.541
0.65	1.550e−02	8.190e−03	460.35	460.65	0.515	0.512
0.8	1.435e−02	5.760e−03	320.78	322.53	0.388	0.385
0.95	1.388e−02	1.710e−03	104.46	111.79	0.130	0.113

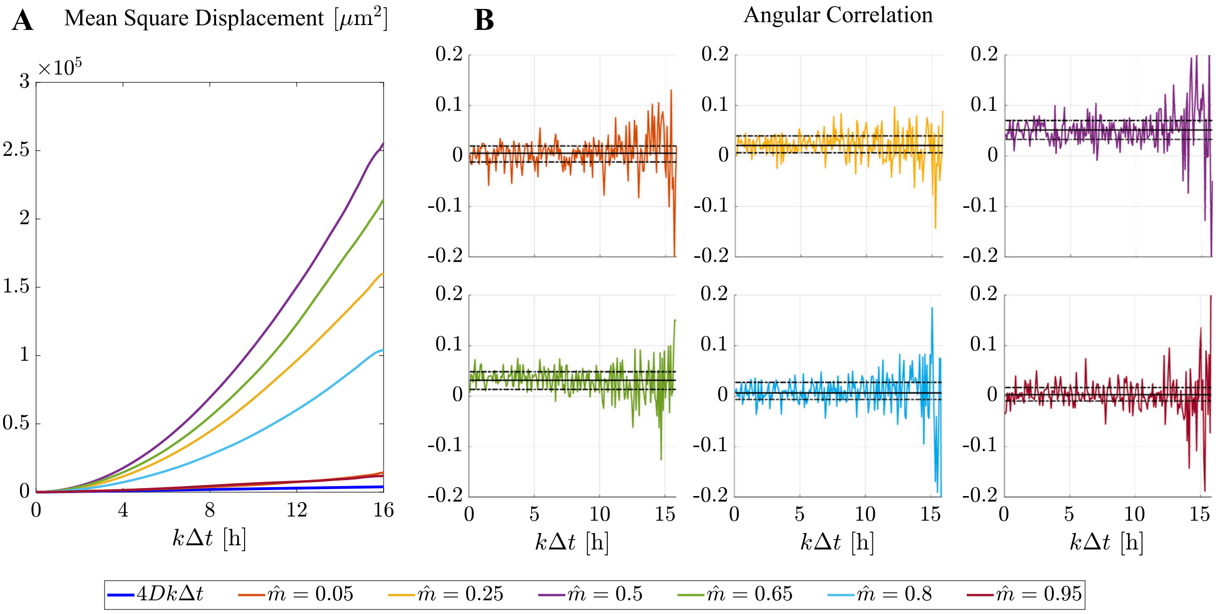

Fig. 7. Quantitative analysis of the numerical outcomes in Fig. 6, where cell dynamics is due to durotaxis. (A) Time evolution of the time-averaged mean square displacement MSD defined in Eq. (28). (B) Time evolution of the temporal angular correlation C defined in Eq. (29). Black horizontal lines denote (starting from the bottom one) the threshold between the first and second quartiles, the means, and the threshold between the third and fourth quartiles.

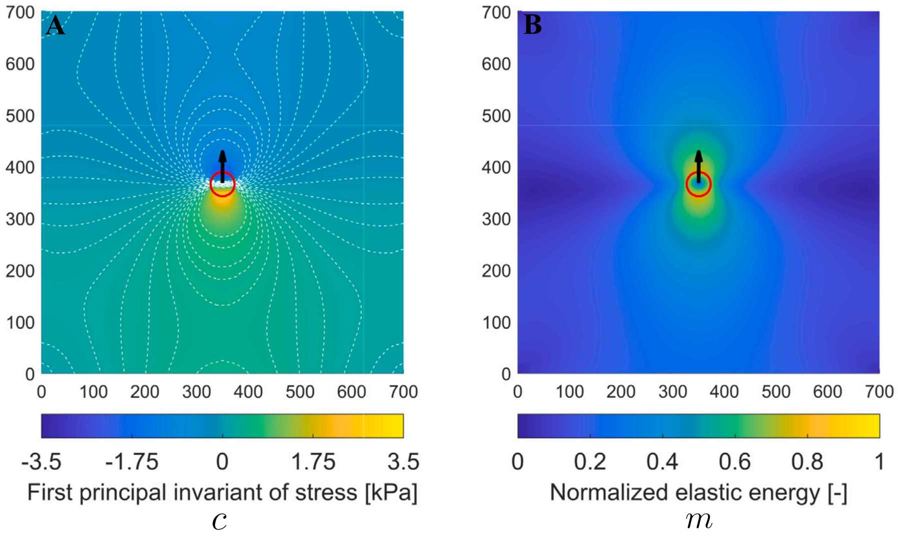

Fig. 8. The first principal invariant of the stress, with its contour lines (white dashed lines), standing for the field c in our tensotaxis model (panel A) and the normalized strain energy representing the field m (panel B) used in the numerical simulations shown in Fig. 9. Specifically, the mechanical behavior of the substrate is here assumed homogeneous with $\hat{\mu}_1 = 2.48$ kPa and $\hat{\mu}_3 = 2.50$ kPa in Eq. (34), while the load in Eq. (15) is applied inside the red circle with magnitude $f_b = 6.1$ kPa and directed upwards, i.e. $\beta = \pi/2$ (black arrow).

Homogeneous mechanical properties of the substrate. The fields μ_1 and μ_3 in Eq. (18), respectively linked to the linear and non-linear mechanical response of the substrate, are first considered homogeneous, i.e.

$$\mu_1(\mathbf{X}) = \hat{\mu}_1, \qquad \mu_3(\mathbf{X}) = \hat{\mu}_3. \tag{34}$$

In this context, we first set $\hat{\mu}_1 = 2.48$ kPa and $\hat{\mu}_3 = 2.50$ kPa, reproducing a polyacrylamide gel (PAG) made with 10% of acrylamide and 0.05% of bis-acrylamide [49], and we assume that the load applied on the substrate has magnitude $f_b = 6.1$ kPa and is directed upwards, i.e. $\beta = \pi/2$ in Eq. (15). We note that the chosen value of $\hat{\mu}_1$, combined with a Poisson ratio $\nu = 0.48$, as reported in Table 2, corresponds to $E \approx 14$ kPa, which is the Young's modulus of the soft substrate used in [15]. However, we note that softer substrates can be found in tensotaxis experiments [31] and in the following we will vary this parameter. The resulting fields c and m, defined in Eqs. (17) and (19) as the first principal invariant of stress and the normalized strain energy density function, respectively, are represented in Fig. 8 in Eulerian coordinates. Notice that c (Fig. 8-A) is almost anti-symmetric with respect to the horizontal line $y = 350$ µm, with positive values under the black circle $\mathcal{D}$, where the traction is applied, and negative values above it. On the other hand, the normalized energy m (Fig. 8-B) is almost symmetric with respect to the same horizontal line, with analogous values either where the substrate is pushed or pulled. In this simulation setup, we first consider different initial conditions to investigate the effect of compressive and tensile stresses on cell dynamics (see Fig. 9). As expected, if the cell is initially placed in the region characterized by positive/tensile stress (see panels A and D in Fig. 9), it polarizes according to the sensed field c and thus moves towards the positive

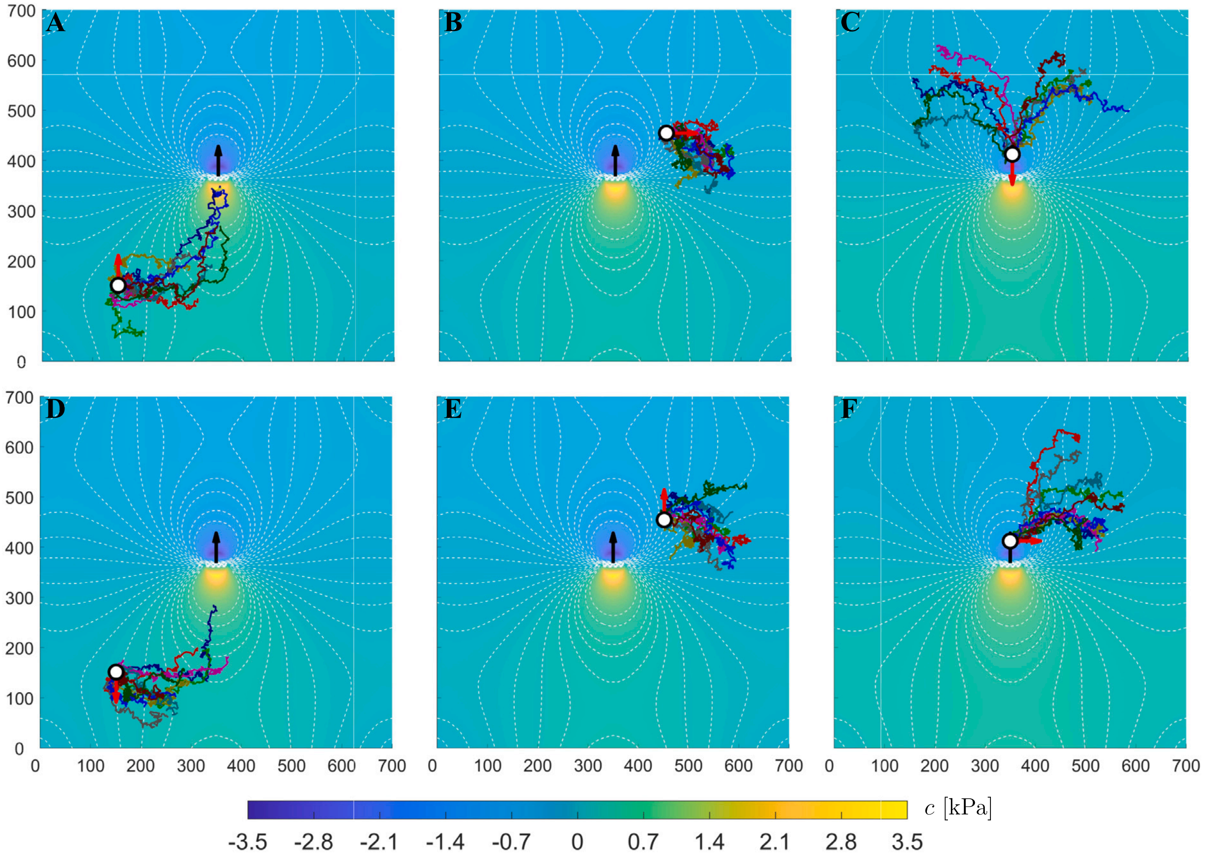

Fig. 9. Numerical simulations reproducing cell dynamics due to tensotaxis in the presence of the fields c and m shown in Fig. 8. The white dashed lines are the contour lines of the first principal invariant of the stress, i.e. c, see Eq. (17). Each panel shows 10 different trajectories starting from different initial locations (white circle) and direction of polarization (red arrows). The considered initial conditions are: (A) $\mathbf{x}_{p,0} = (150, 150)^T$ μm and $\mathbf{w}_0 = (0, 1)^T$; (B) $\mathbf{x}_{p,0} = (450, 450)^T$ μm and $\mathbf{w}_0 = (1, 0)^T$; (C) $\mathbf{x}_{p,0} = (350, 400)^T$ μm and $\mathbf{w}_0 = (0, -1)^T$; (D) $\mathbf{x}_{p,0} = (150, 150)^T$ μm and $\mathbf{w}_0 = (0, -1)^T$; (E) $\mathbf{x}_{p,0} = (450, 450)^T$ μm and $\mathbf{w}_0 = (0, 1)^T$; (F) $\mathbf{x}_{p,0} = (350, 400)^T$ μm and $\mathbf{w}_0 = (1, 0)^T$.

Table 5
Quantitative analysis of the numerical outcomes in Fig. 9. For each case, we report $x_{p,0}$ and $\mathbf{w}_0$ characterizing the initial condition, and the values of the mean speed $\bar{s}$ in Eq. (23), the mean motility $\bar{v}$ in Eq. (24), the overall displacement d^{TOT} and the maximum displacement $d^{\max}$ in Eq. (25), the persistence P in Eq. (26) and the forward migration index FMI in Eq. (27).

$x_{p,0}$ [μm]	$\mathbf{w}_0^T$	$\bar{s}$ [μm/s]	$\bar{v}$ [μm/s]	d^{TOT} [μm]	$d^{\max}$ [μm]	P [−]	FMI [−]
150	(0, 1)	1.413e−02	3.496e−03	183.38	190.39	0.223	0.236
150	(0, −1)	1.404e−02	3.091e−03	156.80	162.74	0.193	0.203
450	(1, 0)	1.396e−02	1.778e−03	106.78	122.70	0.135	0.129
450	(0, 1)	1.372e−02	2.073e−03	129.44	136.02	0.163	0.150
350	(0, −1)	1.406e−02	4.195e−03	215.56	226.62	0.266	0.292
350	(1, 0)	1.403e−02	3.783e−03	194.90	208.08	0.241	0.239

peak of stress at the center of the domain. Conversely, if the cell is initially placed in a region characterized by negative/compressive stress (see panels B, C, E and F in Fig. 9), the cell moves away from the negative peak of c at the center of the domain. This means that the proposed model is able to qualitatively capture the biological observation in [15,31] that the cell is attracted by tensile stresses (panels A and D) and repelled by compressive stresses (panels B, C, E and F). In addition, a comparison between the results in the top and bottom rows in Fig. 9 highlights how the initial cell direction of polarization $\mathbf{w}_0$ affects cell dynamics. It emerges that the initial polarization can lead to a bias in cell direction, without affecting the general behavior, i.e. repulsion from compressive stress and attraction towards tensile one, as well as the value of the output quantities defined in Eqs. (23)–(27) (see Table 5). This is particularly evident in the panels C and F in Fig. 9. In fact, $\mathbf{w}_0 = (-1, 0)^T$ results in a quasi symmetric distribution of cell trajectories (panel C), which is missing if the initial cell polarization $\mathbf{w}_0$ is set to $(0, 1)^T$ (panel F).

We then turn to investigate if and how changes in the magnitude of the exerted load f_b in Eq. (15) and/or the homogeneous mechanical properties of the substrate, i.e. the values of $\hat{\mu}_1$ and $\hat{\mu}_3$ in Eq. (34), affect cell dynamics. In this perspective, the numerical results in Fig. 10 have been obtained by considering

- different force magnitudes, i.e. $f_b = 3.05$ kPa (top row), $f_b = 6.1$ kPa (central row) and $f_b = 12.2$ kPa (bottom row);
- different substrates characterized by the experimental values reported in [49], i.e. $\hat{\mu}_1 = 1.46$ kPa and $\hat{\mu}_3 = 0.25$ kPa (left panels), $\hat{\mu}_1 = 2.48$ kPa and $\hat{\mu}_3 = 2.50$ kPa (central panels), $\hat{\mu}_1 = 4.66$ kPa and $\hat{\mu}_3 = 5.40$ kPa (right panels).

As in previous cases, in all panels, we report 10 distinct realizations of cell trajectory while the relative quantities defined in Eqs. (23)–(27) are listed in Table 6 for $Q = 50$ realizations. Notice that the results in panel E of Fig. 10 have been obtained with the simulation set-up shown in Fig. 9. As a remark, in Fig. 10 we have only shown the field m, since

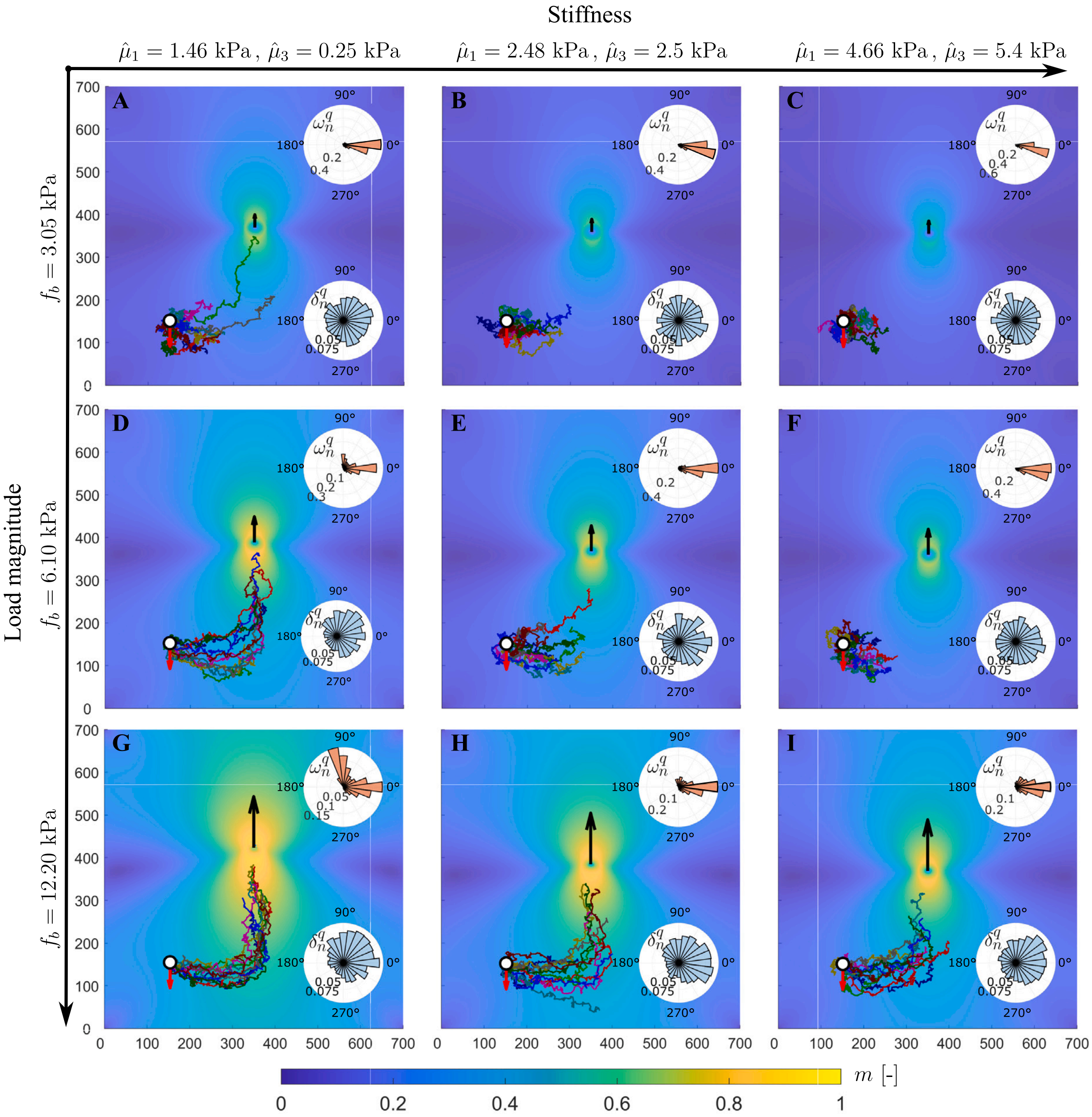

Fig. 10. Numerical simulations reproducing cell dynamics due to tensotaxis in the presence of the fields c and m defined in Eqs. (17) and (19), respectively, with different values of the load magnitude f_b (black arrows), and of the homogeneous substrate mechanical parameters $\hat{\mu}_1$ and $\hat{\mu}_3$. Each panel shows 10 different trajectories starting from the same initial location $\mathbf{x}_{p,0} = (150, 150)^T$ (white circle) with the same direction of polarization $\mathbf{w}_0 = (0, -1)^T$ (red arrows). From top to bottom, the load f_b in Eq. (15) increases assuming the values 3.05 kPa (top row), 6.1 kPa (central row), and 12.2 kPa (bottom row). From left to right the substrate stiffness is increased, by setting: $\hat{\mu}_1 = 1.46$ kPa and $\hat{\mu}_3 = 0.25$ kPa (left panels), $\hat{\mu}_1 = 2.48$ kPa and $\hat{\mu}_3 = 2.50$ kPa (central panels), $\hat{\mu}_1 = 4.66$ kPa and $\hat{\mu}_3 = 5.40$ kPa (right panels). In each panel, the histograms show the distributions of the angles ω_n^q (top) and δ_n^q (bottom) related to the direction of polarization $\mathbf{w}_n^q$ and the actual direction of motion $\mathbf{d}_n^q$, respectively.

variations in the field c due to increases in the applied load f_b or in the values of the mechanical coefficients $\hat{\mu}_1$ and $\hat{\mu}_3$ do not significantly affect the local direction of the gradient of c (see the contour lines in Fig. S9 in the Supplementary Material) and, in turn, the direction of cell trajectories.

These numerical outcomes first highlight that either a decrease in the applied load or an increase in the mechanical properties μ_1 and μ_3 of the substrate (see panels B, C and F in Fig. 10) result in a reduction of cell total displacement (see the values of d^{TOT} and $d^{\max}$ in Table 6) and thus a lower amount of cell trajectories reaches the center of the domain, where the force is applied. Interestingly, this is correlated with a reduction in the motility (see the histograms in Fig. 11 and the values of $\bar{v}$ in Table 6), and very low values of the persistence P and the forward migration index FMI, while the mean speed $\bar{s}$ presents very small fluctuations (see again Table 6). This clearly indicates that a decrease in the applied load and/or an increase in the substrate stiffness consistently result in a reduced cell motility, leading thereby to an almost unbiased Brownian motion of the cell, as confirmed by the linear growth in time $k\Delta t$ of the time-averaged mean square displacement MSD in the panel A of Fig. 11 (see the red dashed and dotted lines and the dotted purple one). Such transition in cell type of motion is due to the fact that either decreasing the applied load or increasing the values of the mechanical coefficients, the strain energy stored in the substrate, and thus m, decreases.

Conversely, either an increase in the applied load or a decrease in the mechanical parameters of the substrate μ_1 and μ_3 (see panels D, G, H in Fig. 10) lead to a higher number of cell trajectories that reach the center of the domain in response to the sensed field m. In fact, as shown by the histograms in Fig. 11 and the values in Table 6, these cases are characterized by an increase in cell motility and a higher

Table 6

Quantitative analysis of the numerical outcomes in Fig. 10. For each case, we report f_b and $\hat{\mu}_1$, characterizing respectively the load magnitude and the mechanical coefficient related to the substrate stiffness, the values of the mean speed $\bar{s}$ in Eq. (23), the mean motility $\bar{v}$ in Eq. (24), the overall displacement d^{TOT} and the maximum displacement $d^{\max}$ in Eq. (25), the persistence P in Eq. (26) and the forward migration index FMI in Eq. (27). The values obtained with the reference fields shown in Fig. 8 are written in bold.

f_b [kPa]	$\hat{\mu}_1$ [kPa]	$\bar{s}$ [μm/s]	$\bar{v}$ [μm/s]	d^{TOT} [μm]	$d^{\max}$ [μm]	P [−]	FMI [−]
3.05	1.46	1.395e−02	2.071e−03	134.91	141.69	0.167	0.158
3.05	2.48	1.372e−02	9.906e−04	75.79	87.27	0.095	0.093
3.05	4.66	1.350e−02	5.514e−04	54.53	66.32	0.071	0.052
6.10	1.46	1.402e−02	4.915e−03	232.00	240.25	0.287	0.357
6.10	**2.48**	**1.386e−02**	**3.056e−03**	**143.51**	**148.37**	**0.180**	**0.186**
6.10	4.66	1.359e−02	1.671e−03	86.21	96.35	0.109	0.098
12.20	1.46	1.504e−02	6.526e−03	261.17	264.02	0.301	0.416
12.20	2.48	1.446e−02	5.514e−03	239.21	244.17	0.287	0.328
12.20	4.66	1.429e−02	4.648e−03	208.86	211.87	0.254	0.284

correlation between cell direction and the stiffness gradient. In other words, as confirmed by the quadratic growth in time $k\Delta t$ of the MSD in Fig. 11 (panel A), cell dynamics is here mainly driven by the external cues rather than by the random term.

Lastly, either a reduction or increase of both the applied load f_b and the substrate stiffness (see panels A and I in Fig. 10) slightly affect the amount of trajectories that reach the positive peak of tension, as well as the type of cell dynamics. In fact, in both cases the time-averaged mean square displacement MSD in Fig. 11 (panel A) quadratically grows in time $k\Delta t$ as in the reference case (see the solid red line, the dotted green line and the dashed purple one, respectively). Moreover, in the case shown in the panel A of Fig. 11, the values of the quantities in Table 6 are very close to those of the reference case, while some small differences are observed in the values relative to the case in panel I of Fig. 11.

In summary, the above observed behaviors are due to the fact that either increasing the applied load or decreasing the values of the mechanical coefficients in a force-controlled experiment, the strain energy stored in the substrate, and thus m, increases. In turn, according to Eq. (20), cell motility increases too (see the mean motility $\bar{v}$ in Table 6 and histograms in panel B of Fig. 11), and so the directional contribution in cell velocity prevails on the Wiener process in Eq. (1). Consequently, cell dynamics change from an almost random walk (see panel C in Fig. 10) to a fully biased motion in which the cell reaches the positive stress peak at the center of the domain (panel G in Fig. 10). This behavior transition is also consistent with the polar histograms in Fig. 10. When the stochastic term prevails (see in particular panels B, C and F), the cell remains in the bottom left part of the domain and so the direction of polarization $\mathbf{w}$ is substantially aligned to the x-axis, while there is no emergence of a preferred direction of motion due to the strength of the random term. Conversely, when the directional contribution in cell velocity prevails (see panels D, G and H), there is a wider variation in the directions of polarization $\mathbf{w}$ as the cell leaves the bottom left part of the domain following the field c. Again the random contributions in cell velocity introduce important differences between the distributions of ω_n^q and δ_n^q. However, the δ_n^q has an asymmetric distribution, that highlights the presence of a preferred direction of motion. Finally, the time evolution of the temporal angular correlation $C(k\Delta t)$ is not shown here since in all cases its average is approximately null. This indicates that, in all cases, there is no correlation between the variations of the direction of motion. This result is related to the fact that cell direction progressively changes following the field c, in addition to being constantly affected by the random term.

Inhomogeneous mechanical properties of the substrate. Lastly, we turn to assume that the mechanical parameters of the substrate, μ_1 and μ_3, are inhomogeneous in space. This allows us to test our model in a more complex setting, which could be relevant in some biological applications (e.g. scar formation, wound healing, bone repair, fibrosis) and in tissue engineering, although to our knowledge no experiments of this type have been performed in the literature. In particular, we consider a set-up in which the left side of the undeformed substrate is characterized by the mechanical coefficients $\hat{\mu}_1^L$ and $\hat{\mu}_3^L$, and the right side by $\hat{\mu}_1^R$ and $\hat{\mu}_3^R$, by setting in the reference configuration

$$\mu_1(\mathbf{X}) = \begin{cases} \hat{\mu}_1^L & \text{if} \quad X \in [0, d_3 - \delta], \\ S_5(X) & \text{if} \quad X \in (d_3 - \delta, d_3 + \delta), \\ \hat{\mu}_1^R & \text{if} \quad X \in [d_3 + \delta, L], \end{cases} \tag{35}$$

and

$$\mu_3(\mathbf{X}) = \begin{cases} \hat{\mu}_3^L & \text{if} \quad X \in [0, d_3 - \delta], \\ S_6(X) & \text{if} \quad X \in (d_3 - \delta, d_3 + \delta), \\ \hat{\mu}_3^R & \text{if} \quad X \in [d_3 + \delta, L], \end{cases} \tag{36}$$

being S_5 and S_6 proper third-degree polynomials that guarantee the differentiability of the fields μ_1 and μ_3. The values of d_3 and δ used in the following simulations have been set to 280 μm and 20 μm, respectively, to avoid that the load, applied in the circle $\mathcal{D}$ at the center of the substrate, falls in the transition region. In order to prevent numerical issues due to the smoothing of the fields, we here use a thicker regular grid $\Lambda \times \Lambda$ with $\Lambda = 350$ (see Section 3).

In this context, we firstly consider a substrate with a stiffer region on its right side, which is thus characterized by higher mechanical properties than the left one. Specifically, referring to the experimental range reported in [49] and considering Eqs. (35) and (36), we set $\hat{\mu}_1^L = 1.46$ kPa and $\hat{\mu}_3^L = 0.25$ kPa for the softer (left) side of the substrate, and $\hat{\mu}_1^R = 4.66$ kPa and $\hat{\mu}_3^R = 5.4$ kPa on the stiffer (right) side. In this substrate setup, the numerical outcomes in panels A and C of Fig. 12 show cell dynamics when a load with magnitude $f_b = 6.1$ kPa and pulling upwards, i.e. with $\beta = \pi/2$ in Eq. (15), is applied to the substrate in $\mathcal{D}$ (which here falls in the right stiffer side of the ECM), with different initial position of the cells. In particular, we notice that despite the gradient of the volumetric stress, represented by the first principal invariant of the Cauchy stress tensor (see the dashed white lines), is higher on the stiffer (right) part of the substrate, the results are qualitatively similar to the homogeneous setup of Fig. 9. The cell tends in fact to move towards tensile stresses and away from compressive ones. We remark that in this case, since we have not explicitly included the motion due to durotaxis, the cell tends to stay on the softer side if the stiffer region close to the cell is compressed (panel C in Fig. 12).

We then turn to consider a substrate whose left side is much stiffer, i.e. it is characterized by higher mechanical properties than the right one. In particular, always referring to the experimental range reported in [49], we set $\hat{\mu}_1^L = 4.66$ kPa, $\hat{\mu}_3^L = 5.4$ kPa, $\hat{\mu}_1^R = 1.46$ kPa and $\hat{\mu}_3^R = 0.25$ kPa in Eqs. (35) and (36). In this new setting, we still consider the same external force and initial conditions as the previous case, so that the load is applied on the softer part of the substrate. The numerical outcomes in panels B and D of Fig. 12 show that, even though the cell continues to move towards tensile stresses, its trajectory is here influenced also by the inhomogeneity of the substrate, specifically

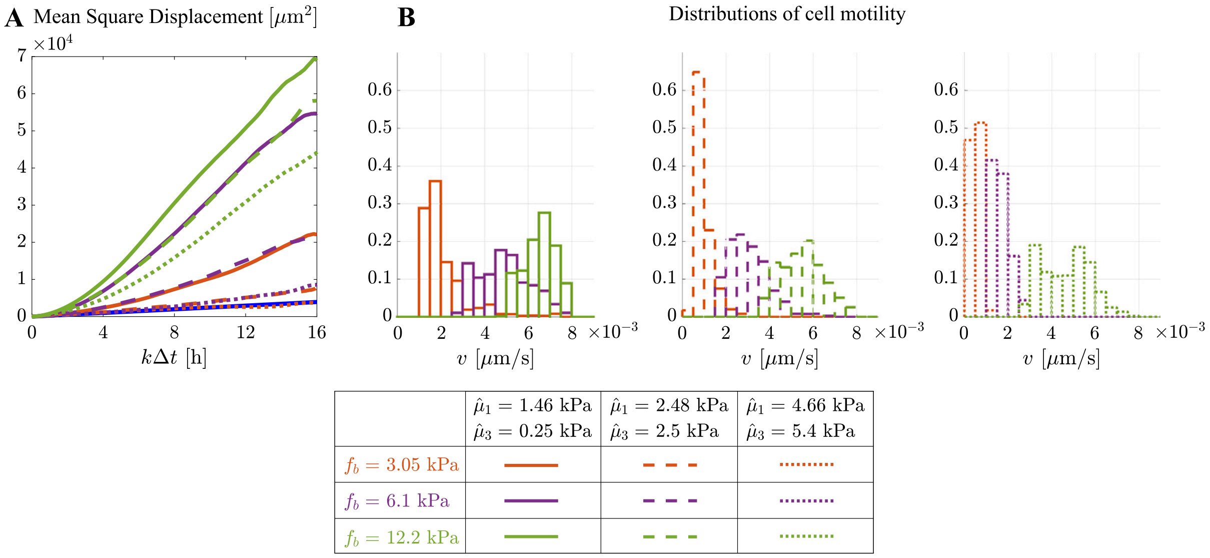

Fig. 11. Quantitative analysis of the numerical outcomes in Fig. 10. (A) Temporal evolution of the time-averaged mean square displacement MSD defined in Eq. (28). The blue solid line is the straight line $4Dk\Delta t$ characteristic of the Brownian motion. (B) Histograms showing the values of cell motility v.

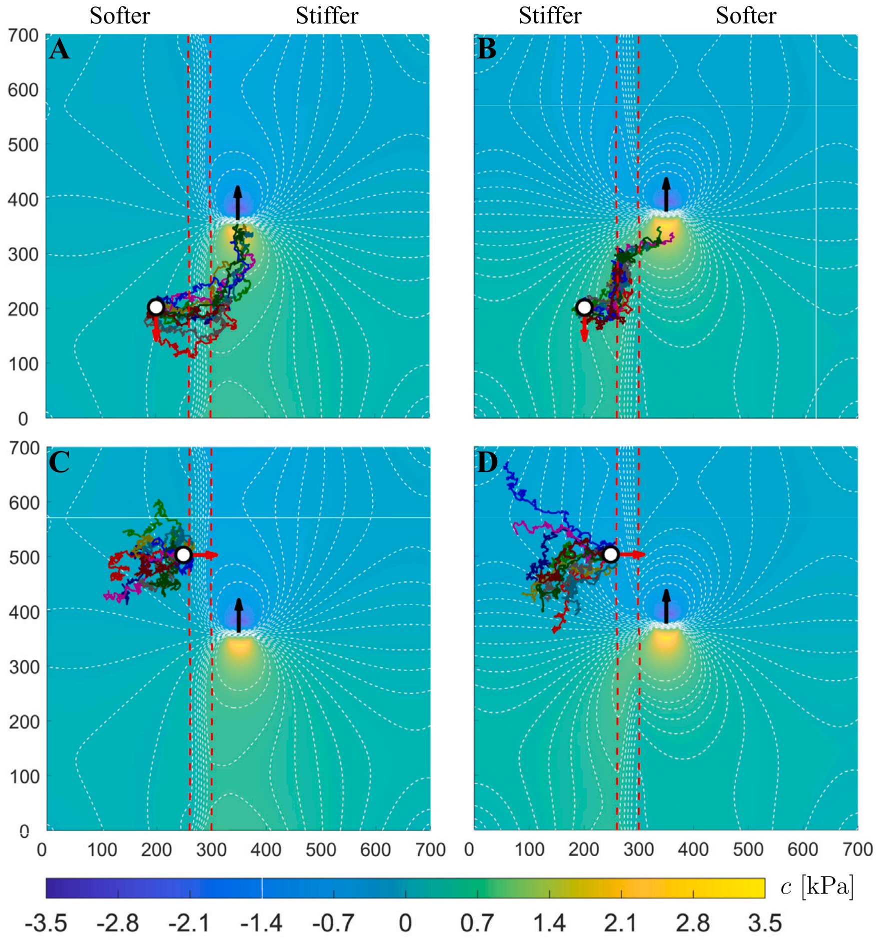

Fig. 12. Numerical simulations reproducing cell dynamics due to tensotaxis in the case of an inhomogeneous substrate, i.e. by setting $\hat{\mu}_1^L = 1.46$ kPa, $\hat{\mu}_3^L = 0.25$ kPa, $\hat{\mu}_1^R = 4.66$ kPa and $\hat{\mu}_3^R = 5.4$ kPa in Eqs. (35) and (36) in panels A and C, and $\hat{\mu}_1^L = 4.66$ kPa, $\hat{\mu}_3^L = 5.4$ kPa, $\hat{\mu}_1^R = 1.46$ kPa and $\hat{\mu}_3^R = 0.25$ kPa in panels B and D. The substrate is pulled upwards in $\mathcal{D}$ with $f_b = 6.1$ kPa (black arrows). Each panel shows 10 different trajectories starting from different initial conditions (as indicated by the white circles and the red arrows): (A and B) $\mathbf{x}_{p,0} = (200, 200)^T$ µm and $\mathbf{w}_0 = (0, -1)^T$, (C and D) $\mathbf{x}_{p,0} = (250, 500)^T$ µm and $\mathbf{w}_0 = (1, 0)^T$. The white dashed lines are the contour lines of the first principal invariant of the stress, i.e. of c. The red dashed lines define the transition zone of the mechanical coefficients μ_1 and μ_3.

when the cell is initially placed on the stiffer side (panel B in Fig. 12). Indeed, in this case, the cell tends to move alongside the transition zone, while migrating towards the tensile region. Furthermore, very few cell trajectories reached the most stretched region in the time lapse

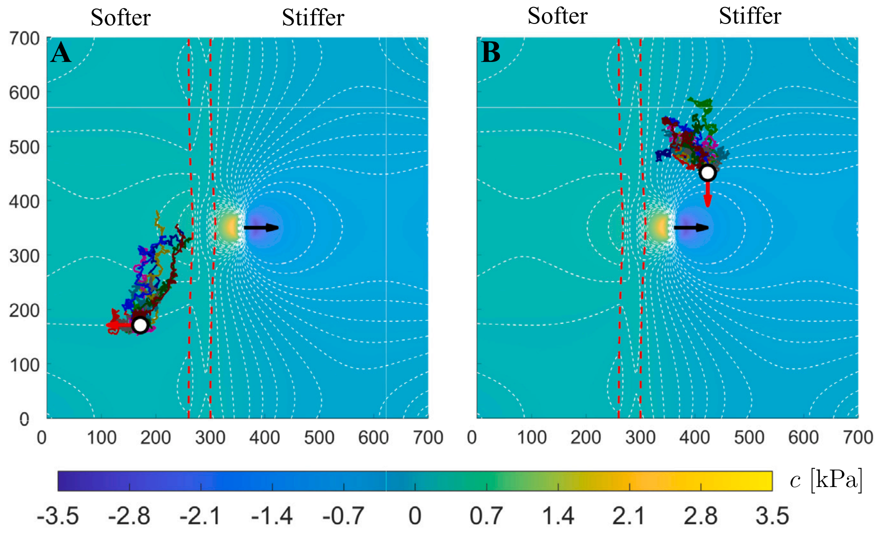

Fig. 13. Numerical simulations reproducing cell dynamics due to tensotaxis in the case of an inhomogeneous substrate, i.e. by setting $\hat{\mu}_1^L = 1.46$ kPa, $\hat{\mu}_3^L = 0.25$ kPa, $\hat{\mu}_1^R = 4.66$ kPa and $\hat{\mu}_3^R = 5.4$ kPa in Eqs. (35) and (36) as in panels A and C of Fig. 12. The substrate is pulled horizontally, with $\beta = 0$, in D with $f_b = 6.1$ kPa (black arrows). Each panel shows 10 different trajectories with the following initial conditions (white circles and red arrows): (A) $\mathbf{x}_{p,0} = (170, 170)^T$ μm and $\mathbf{w}_0 = (0, -1)^T$; (B) $\mathbf{x}_{p,0} = (420, 450)^T$ μm and $\mathbf{w}_0 = (0, -1)^T$. The white dashed lines are the contour lines of the first principal invariant of the stress, i.e. of c. The red dashed lines define the transition zone of the mechanical coefficients μ_1 and μ_3.

of the numerical simulations, while in the other realizations the cell persists to migrate on the stiffer side or on the transition zone.

Lastly, in Fig. 13 we consider the same substrate setup used in the panels A and C of Fig. 12, but we here assume that the load, applied on the stiffer right side, is horizontally directed towards the right, by setting $\beta = 0$ in Eq. (15). In panel A of Fig. 13, we observe that the cell, initially placed on the softer left side, tends to stay there driven by the field c. In this case, the most tensed region (i.e. where the first principal invariant of the stress is maximum) located on the stiffer side of the substrate, is never reached by the cell in any of the ten realizations. On the other hand, in panel B of Fig. 13 it is possible to see that if the cell is initially placed on the stiffer (right) side of the substrate, which is compressed, it is repelled, as expected, by the compressive stresses.

We remark, however, that in all these cases a possible combined effect between durotaxis and tensotaxis is disregarded and, thus, the inhomogeneous setting deserves further mathematical modeling efforts possibly supported by biological experiments.

5. Conclusions and perspectives

We have presented a new phenomenological model for cell migration on 2D substrates in response to mechanical stimuli, adapted from the chemotactic model proposed in [48]. In our model, a single representative cell changes its motility and its direction of polarization sensing different mechanical cues in a non-local and non-isotropic way. We specialize our model to describe durotaxis, i.e. the motion towards stiffer regions of the substrate, and tensotaxis, i.e. the motion towards tensile stresses and away from compressive stresses of the substrate itself. After having proved the existence and uniqueness of the solution, under proper assumptions, the model is numerically solved by considering different biologically relevant settings. Interestingly, the numerical outcomes reported in the paper qualitatively agree with the experimental observations. Specifically, the model is able to reproduce both cells movements in response to rigidity gradients of the substrate and cells preference for stiffer matrices with respect to softer ones, as shown in durotaxis experiments [15,30]. Moreover, when tensotaxis is concerned, the model is able to qualitatively capture cell motion towards tensile stresses and away from compressive ones, accordingly to the biological observations reported in [5,15,34,36,38,39].

However, our study has some simplifications and limitations, which might be interesting to address in future works. From the modeling point of view, the proposed model is purely phenomenological, and does not take into account the subcellular mechanisms involved in the migration process. In this respect, the model should be further refined to link the macroscopic field c and m sensed by the cell to subcellular pathways, by defining a multiscale or nested model able to capture phenomena occurring at the molecular and cellular scales.

Future works should also focus on the mechanical interaction between the cell and the substrate, which has been neglected in the present model. Indeed, it is well know that, while moving, cells exert traction forces on the substrate they are anchored on [80–82]. This visco-elastic interaction should be taken into account since it modifies stresses and strains within both the substrate and the cell itself [83]. This could be possibly captured by our model by including the description of the mechanical forces exchanged between the cell and the substrate, within the sensing region. The inclusion of this mechanical feedback can also allow to describe the changes in cell shape, as well as in the distribution of FAs. We remark that in this case, we should also address time dependent forces and mechanical cues, too. The cell migration model already accounts for possible time dependence of the fields c and m. Even though the mechanical problem for the substrate manipulation can, in principle, involve a load that varies over time, this will lead to a time-dependent deformation of the substrate. This aspect should be addressed within the numerical implementation of the model, since the grid would deform at each different time step. Therefore, the time step for the cell dynamics and the mechanical manipulation of the substrate problems should be carefully set. Furthermore, the spatial interpolation of the evolving fields c and m should also be taken into account, and the quadrature formulas used to compute the integrals M in Eq. (3) and $\mathbf{W}$ in Eq. (6) should be specialized for the case of an evolving grid. The modification of the numerical scheme to handle also time dependent cues will be fundamental also to describe cell migration in response to mechanical stimuli occurring during embryogenesis and morphogenesis, for instance [84].

Moreover, the simulations we have performed aimed to reproduce the processes of durotaxis and tensotaxis, treating them separately. However, they likely involve similar or analogous subcellular mechanisms and they should be treated congruently and perhaps simulated simultaneously. In general, since cells migrating *in vivo* are exposed to an environment characterized by a combination of biochemical, biophysical, and topological cues, it is likely that cells migrate by performing a sort of “mixotaxis” [85], and it would be interesting to consider more signals in our model, changing properly the fields c and m, or considering different choices of the function f.

Finally, the present work should be regarded as a proof of concept of a simple phenomenological model for cell motion in response to mechanical cues and it needs to be tested with experimental tests performed ad hoc using engineered substrates with prescribed mechanical properties [76,86].

CRediT authorship contribution statement

Roberto Marchello: Formal analysis, Investigation, Methodology, Software, Writing – original draft, Writing – review & editing. **Annachiara Colombi:** Conceptualization, Formal analysis, Investigation, Methodology, Software, Writing – original draft, Writing – review & editing. **Luigi Preziosi:** Conceptualization, Funding acquisition, Investigation, Methodology, Supervision, Writing – original draft, Writing – review & editing. **Chiara Giverso:** Conceptualization, Formal analysis, Investigation, Methodology, Software, Supervision, Writing – original draft, Writing – review & editing.

Declaration of competing interest

All authors declare that they have no affiliations with or involvement in any organization or entity with any financial interest, or non-financial interest in the subject matter discussed in this manuscript.

Acknowledgments

This work has been partially supported by the Italian Ministry of University and Research through the *Research Project of National Interest* PRIN2017 n. 2017KL4EF3 and PRIN2020 n. 2020F3NCPX. The authors are members of the National Group of Mathematical Physics (GNFM) of the Italian Institute for High Mathematics (INdAM). AC acknowledges the support of GNFM–INdAM through the project *Progetto Giovani 2023* CUP_E53C22001930001.

Appendix A. Analytical results

In this section, the existence and uniqueness of the solution of the model proposed in Section 2.1, and its dependence on the initial condition under a minimal set of assumptions (satisfied by the functions considered in Section 4) are proved. In particular, we will first recall two preliminary results regarding Eq. (4), that will be fundamental for the subsequent proof. The proofs of these results can be found in [48], where the same equation for the evolution of the polarization vector has been used. Then we will state details on the notation, and we will list the considered set of assumptions that allows to prove the existence and uniqueness of the solution of the model proposed in this work, that substantially differs from [48] due to the introduction of the stochastic term in Eq. (1), the definition of the cell preferred axis given by Eq. (6), and the choice of the functional form of the kernels K_r and K_θ, which requires special attention in the proof.

A.1. Preliminary results

Proposition 1. *If the initial polarization vector* $\mathbf{w}(0)$ *is such that* $\|\mathbf{w}(0)\| =: w_0 \in (0,1]$*, Eq. (4) ensures that cell polarization* $\mathbf{w}(t)$ *has* $\|\mathbf{w}(t)\| \le 1$ *for any* $t > 0$*.*

Proposition 2. *For any* $\mathbf{w}_1, \mathbf{w}_2 \in \mathbb{R}^2$ *such that* $\|\mathbf{w}_1\|, \|\mathbf{w}_2\| \ge w_0$*, with* $w_0 \in (0,1]$*, there exists a constant* $C_{w_0} > 0$ *such that*

$$\left\| \frac{\mathbf{w}_1}{\|\mathbf{w}_1\|} - \frac{\mathbf{w}_2}{\|\mathbf{w}_2\|} \right\| \le C_{w_0} \|\mathbf{w}_1 - \mathbf{w}_2\|. \tag{A.1}$$

A.2. Notation

The substrate on which the cell migrates is identified with an open and connected set $\Omega \subseteq \mathbb{R}^2$, while the set of possible cell positions is defined as $\mathcal{X} := \{\mathbf{x}_p \in \mathbb{R}^2 \mid \mathcal{S}(\mathbf{x}_p) \subseteq \Omega\}$, being $\mathcal{S}(\mathbf{x}_p)$ the circle centered at $\mathbf{x}_p$ and with radius $R > 0$. According to [48], we define the time interval $\mathcal{I} := [0,T]$ such that, given the initial condition $\mathbf{w}(0)$ with $\|\mathbf{w}(0)\| = w_0 \in (0,1]$, the cell direction of motion satisfies $\|\mathbf{w}(t)\| \ge w_0$ and $\mathbf{x}_p \in \mathcal{X}$ for any $t \in \mathcal{I}$. Moreover, referring to Proposition 2, we denote by $\mathcal{D}$ the set of possible cell polarization vectors, i.e. $\mathcal{D} := \{\mathbf{w} \in \mathbb{R}^2 \text{ such that } \|\mathbf{w}\| \in [w_0, 1]\} \subset \mathbb{R}^2$. Cell speed $v(t)$ is hereafter denoted by $v(t, \mathbf{x}_p, \mathbf{w})$ in order to remark that it depends on the present position $\mathbf{x}_p(t)$ and the polarization vector $\mathbf{w}(t)$ of the cell, see Eqs. (2). Lastly, we introduce $\mathbf{z}(t) := (\mathbf{x}_p(t), \mathbf{w}(t))^T \in \mathcal{X} \times \mathcal{D}$ and denote by $\|\cdot\|_{2\times 2}$ the norm on $\mathbb{R}^2 \times \mathbb{R}^2$ defined by $\|\mathbf{z}\|_{2\times 2} := \|\mathbf{x}_p\| + \|\mathbf{w}\|$.

The proposed model constituted by Eqs. (1)–(2), enriched by proper explicit functional forms of the function f, the kernels K_r and K_θ, and the fields m and c, is rewritten in the following canonical form

$$\begin{cases} \mathrm{d}\mathbf{z}(t) = \mathbf{F}(t, \mathbf{z}(t))\,\mathrm{d}t + \begin{pmatrix} \sqrt{2D}\,\mathrm{d}\mathbf{B}(t) \\ \mathbf{0} \end{pmatrix}, \quad \text{for } t \in (0,T], \\ \mathbf{z}(0) = \mathbf{z}_0, \end{cases} \tag{A.2}$$

where $\mathbf{z}_0 := (\mathbf{x}_p(0), \mathbf{w}(0))^T \in \mathcal{X} \times \mathbb{R}^2$ is an initial condition such that $\|\mathbf{w}(0)\| \le 1$; while

$$\mathbf{F}(t, \mathbf{z}(t)) := (\mathbf{g}_\mathbf{x}(t, \mathbf{x}_p(t), \mathbf{w}(t)), \mathbf{g}_\mathbf{w}(t, \mathbf{x}_p(t), \mathbf{w}(t)))^T, \tag{A.3}$$

being $\mathbf{g}_\mathbf{x}(t, \mathbf{x}_p(t), \mathbf{w}(t)) := v(t)\mathbf{w}(t)$ and $\mathbf{g}_\mathbf{w}(t, \mathbf{x}_p(t), \mathbf{w}(t))$ the right hand side of Eq. (4). Then $\mathbf{Z}(t) \in \mathcal{X} \times \mathcal{D}$ is hereafter said solution for any $t \in \mathcal{I}$ of Eq. (A.2) in the sense of the following Definition.

Definition 1. Let $\{\mathbf{B}(t)\}_{t\in\mathcal{I}}$ be a two dimensional vector Wiener process on a probability space $(\Omega, \mathcal{F}, P)$ with an admissible filtration $\mathbb{F} = \{\mathcal{F}\}_{t\ge 0}$. A solution of the stochastic differential equation (A.2) with initial condition $\mathbf{z}_0 = (\mathbf{x}_p(0), \mathbf{w}(0))^T \in \mathcal{X} \times \mathbb{R}^2$ with $w_0 := \|\mathbf{w}(0)\| \le 1$ is an adapted process $\mathbf{Z}(t)$ with continuous paths such that for all $t \in \mathcal{I}$

$$\mathbf{Z}(t) = \mathbf{z}_0 + \int_0^t \mathbf{F}(s, \mathbf{Z}(s))\,\mathrm{d}s + \begin{pmatrix} \int_0^t \sqrt{2D}\,\mathrm{d}\mathbf{B}(s) \\ \mathbf{0} \end{pmatrix}, \tag{A.4}$$

being $\int_0^t \sqrt{2D}\mathrm{d}\mathbf{B}(s)$ an Ito’s stochastic integral [53].

A.3. Assumptions

Assumption 1. Let $m : \mathcal{I} \times \Omega \mapsto [0,1]$ in Eq. (3) be a Lipschitz continuous function on Ω, i.e. there exists a constant $Lip(m) > 0$ such that

$$|m(t, \mathbf{x}_1) - m(t, \mathbf{x}_2)| \le Lip(m)\, \|\mathbf{x}_1 - \mathbf{x}_2\|,$$

for every $\mathbf{x}_1, \mathbf{x}_2 \in \Omega$ and $t \in \mathcal{I}$.

Assumption 2. Let $c : \mathcal{I} \times \Omega \mapsto \mathbb{R}$ in Eq. (6) be a function bounded and Lipschitz continuous on Ω, i.e. there exist two constants $c_0 > 0$ and $Lip(c) > 0$ such that $|c(t, \mathbf{y})| \le c_0$ and

$$|c(t, \mathbf{x}_1) - c(t, \mathbf{x}_2)| \le Lip(c)\, \|\mathbf{x}_1 - \mathbf{x}_2\|,$$

for every $\mathbf{x}_1, \mathbf{x}_2 \in \Omega$ and $t \in \mathcal{I}$.

Assumption 3. Let $K_\theta : [-1,1] \mapsto [0,1]$ in Eq. (8) write as

$$K_\theta(u) = \begin{cases} K_\theta^+(u), & \text{if } u \in [\alpha, 1], \\ 0, & \text{if } u \in (-\alpha, \alpha), \\ K_\theta^-(u), & \text{if } u \in [-1, -\alpha], \end{cases}$$

with $\alpha \in [0,1)$. In particular, $K_\theta^+ : [\alpha, 1] \mapsto [0,1]$ has compact support and is Lipschitz continuous over $[\alpha, 1]$, i.e. there exists a constant $Lip(K_\theta^+) > 0$ such that

$$|K_\theta^+(u_1) - K_\theta^+(u_2)| \le Lip(K_\theta^+)|u_1 - u_2|,$$

for every $u_1, u_2 \in [\alpha, 1]$. Moreover, $K_\theta^- : [-1, -\alpha] \mapsto [0, 1]$ has compact support and is Lipschitz continuous over it, i.e. there exists a constant $Lip(K_\theta^-) > 0$ such that

$$|K_\theta^-(u_1) - K_\theta^-(u_2)| \leq Lip(K_\theta^-)|u_1 - u_2|,$$

for every $u_1, u_2 \in [-1, -\alpha]$.

Assumption 4. Let $\mathbf{z}_0 := (\mathbf{x}_p(0), \mathbf{w}(0))^T$ in Eq. (A.2) be such that $\|\mathbf{w}(0)\| =: w_0 \in (0, 1]$ and $\mathbf{x}_p(0) \in \mathcal{X}$.

Assumption 5. Let $f : [0, 1] \mapsto [0, 1]$ in Eq. (2) be a Lipschitz continuous function on $[0, 1]$, i.e. there exists a constant $Lip(f) > 0$ such that

$$|f(u_1) - f(u_2)| \leq Lip(f)|u_1 - u_2|,$$

for every $u_1, u_2 \in [0, 1]$.

Remark 1. We remark that the kernel $K_r : [0, R] \mapsto [0, 1]$ in Eq. (8) is assumed to be properly defined to result in a Riemann integrable function.

Remark 2. We remark that the random term in Eq. (1) is given by the constant parameter $\sqrt{2D} \in \mathbb{R}$ and the vector Wiener process $\mathbf{B}(t)$.

A.4. Main analytical result

Theorem 1. *If the system defined in Eq. (A.2) (and specified in Eqs. (1)–(8)) satisfies Assumptions 1–5, the following statements hold true:*

1. *(Lipschitz continuity of* $\mathbf{F}$*)* $\mathbf{F} : \mathcal{I} \times \mathcal{X} \times \mathcal{D} \mapsto \mathbb{R}^2 \times \mathbb{R}^2$ *is Lipschitz continuous on* $\mathcal{X} \times \mathcal{D}$ *for any* $t \in \mathcal{I}$;
2. *(existence and uniqueness) Eq. (A.2) admits unique stochastic process* $\mathbb{Z}(t) \in \mathcal{X} \times \mathcal{D}$ *solution on* $\mathcal{I}$ *in the sense of Definition 1;*
3. *(dependence on the initial condition) let* $\mathbf{Z}_1(t) = (\mathbf{x}_{p1}(t), \mathbf{w}_1(t))^T : \mathcal{I} \mapsto \mathcal{X} \times \mathcal{D}$ *and* $\mathbf{Z}_2(t) = (\mathbf{x}_{p2}(t), \mathbf{w}_2(t))^T : \mathcal{I} \mapsto \mathcal{X} \times \mathcal{D}$ *denote two cell trajectory–polarization pairs obtained when the initial condition is set equal to* $\mathbf{z}_{0,1} := (\mathbf{x}_{p1}(0), \mathbf{w}_1(0))^T \in \mathcal{X} \times \mathcal{D}$ *and* $\mathbf{z}_{0,2} := (\mathbf{x}_{p2}(0), \mathbf{w}_2(0))^T \in \mathcal{X} \times \mathcal{D}$*, respectively, it then results that*

$$\|\mathbf{Z}_1(t) - \mathbf{Z}_2(t)\|_{2\times 2} \leq \exp(\mathrm{Lip}(\mathbf{F})\, t)\; \|\mathbf{z}_{0,1} - \mathbf{z}_{0,2}\|_{2\times 2}, \tag{A.5}$$

for any $t \in \mathcal{I}$.

Proof. We first recall that Ito's existence and uniqueness theorem (see [53]) and the Grönwall's Lemma ensure that the Lipschitz continuity of $\mathbf{F}$ implies Statement 2, since the random term in Eq. (1) is an additive noise (see the Remark 2). In this respect, we will prove Statements 1 and 3, only.

Proof of Statement 1. The proof of Statement 1 consists in three different steps.

Step 1. Lipschitz continuity of $\mathbf{F}$. First, we remark that $\mathbf{F} : \mathcal{I} \times \mathcal{X} \times \mathcal{D} \mapsto \mathbb{R}^2 \times \mathbb{R}^2$ is Lipschitz continuous on $\mathcal{X} \times \mathcal{D}$ for any $t \in \mathcal{I}$, if its components $\mathbf{g}_\mathbf{x} : \mathcal{I} \times \mathcal{X} \times \mathcal{D} \mapsto \mathbb{R}^2$ and $\mathbf{g}_\mathbf{w} : \mathcal{I} \times \mathcal{X} \times \mathcal{D} \mapsto \mathbb{R}^2$ (defined in Eqs. (1) and (4), respectively) are both Lipschitz continuous on $\mathcal{X} \times \mathcal{D}$ for any $t \in \mathcal{I}$. We therefore focus on each component, separately.

Step 2. Lipschitz continuity of $\mathbf{g}_\mathbf{x}$. For any $t \in \mathcal{I}$, $\mathbf{x}_{p1}, \mathbf{x}_{p2} \in \mathcal{X}$ and $\mathbf{w}_1, \mathbf{w}_2 \in \mathcal{D}$, we have that

$$\begin{aligned}\|\mathbf{g}_\mathbf{x}(t, \mathbf{x}_{p1}, \mathbf{w}_1) - \mathbf{g}_\mathbf{x}(t, \mathbf{x}_{p2}, \mathbf{w}_2)\| &= \|v(t, \mathbf{x}_{p1}, \mathbf{w}_1)\mathbf{w}_1 - v(t, \mathbf{x}_{p2}, \mathbf{w}_2)\mathbf{w}_2\| \\ &\leq |v(t, \mathbf{x}_{p1}, \mathbf{w}_1)|\, \|\mathbf{w}_1 - \mathbf{w}_2\| + |v(t, \mathbf{x}_{p1}, \mathbf{w}_1) - v(t, \mathbf{x}_{p2}, \mathbf{w}_2)|\, \|\mathbf{w}_2\|.\end{aligned} \tag{A.6}$$

Recalling the definition of cell speed v in Eq. (2) and that $f : [0, 1] \mapsto [0, 1]$, it results that $|v(t, \mathbf{x}_p, \mathbf{w})| \leq V_M$ for any $(t, \mathbf{x}_p, \mathbf{w}) \in \mathcal{I} \times \mathcal{X} \times \mathcal{D}$. Moreover, we have

$$\begin{aligned}&|v(t, \mathbf{x}_{p1}, \mathbf{w}_1) - v(t, \mathbf{x}_{p2}, \mathbf{w}_2)| \leq V_\mathrm{M}\, \mathrm{Lip}(f)\, |M(t, \mathbf{x}_{p1}, \mathbf{w}_1) - M(t, \mathbf{x}_{p2}, \mathbf{w}_2)| \\ &\leq \underbrace{V_\mathrm{M}\, \mathrm{Lip}(f)\, \mathrm{Lip}(M)}_{=:\, \mathrm{Lip}(v)} \Big(\|\mathbf{x}_{p1} - \mathbf{x}_{p2}\| + \|\mathbf{w}_1 - \mathbf{w}_2\| \Big),\end{aligned} \tag{A.7}$$

where the first inequality results from the Lipschitz continuity of f (see Assumption 5); while the latter follows from the Lipschitz continuity of m (see Assumption 1), as it implies the Lipschitz continuity of M (see Eq. (A.7) in [48] for further details). Eq. (A.6) therefore reads as

$$\begin{aligned}&\|\mathbf{g}_\mathbf{x}(t, \mathbf{x}_{p1}, \mathbf{w}_1) - \mathbf{g}_\mathbf{x}(t, \mathbf{x}_{p2}, \mathbf{w}_2)\| \\ &\leq \underbrace{V_M\, (1 + \mathrm{Lip}(f)\, \mathrm{Lip}(M))}_{\mathrm{Lip}(\mathbf{g}_\mathbf{x})} \Big(\|\mathbf{x}_{p1} - \mathbf{x}_{p2}\| + \|\mathbf{w}_1 - \mathbf{w}_2\| \Big).\end{aligned} \tag{A.8}$$

Step 3. Lipschitz continuity of $\mathbf{g}_\mathbf{w}$. For any $t \in \mathcal{I}$, $\mathbf{x}_{p1}, \mathbf{x}_{p2} \in \mathcal{X}$ and $\mathbf{w}_1, \mathbf{w}_2 \in \mathcal{D}$, it results

$$\begin{aligned}&\Big\|\mathbf{g}_\mathbf{w}(t, \mathbf{x}_{p1}, \mathbf{w}_1) - \mathbf{g}_\mathbf{w}(t, \mathbf{x}_{p2}, \mathbf{w}_2)\Big\| \\ &\leq \frac{1}{\tau} \left(\frac{2\|\mathbf{W}(t, \mathbf{x}_{p2}, \mathbf{w}_2)\| + \varepsilon}{\varepsilon^2}\, \|\mathbf{W}(t, \mathbf{x}_{p1}, \mathbf{w}_1) - \mathbf{W}(t, \mathbf{x}_{p2}, \mathbf{w}_2)\| \right. \\ &\left. + \|\mathbf{w}_1 - \mathbf{w}_2\| \right),\end{aligned} \tag{A.9}$$

being $\varepsilon > 0$ (see Eqs. (A.10) and (A.11) in [48] for further details). It is then straightforward to verify that the boundedness of c, K_θ and K_r implies the boundedness of $\mathbf{W}$, i.e. it results $\|\mathbf{W}(t, \mathbf{x}_p, \mathbf{w})\| \leq 2c_0\pi R^2$ for any $(t, \mathbf{x}_p, \mathbf{w}) \in \mathcal{I} \times \mathcal{X} \times \mathcal{D}$.

Concerning instead the second norm in Eq. (A.9), the Lipschitz continuity of $\mathbf{W}$ follows from the boundedness and Lipschitz continuity of c (Assumption 2), the boundedness and Lipschitz continuity of K_θ^+ and K_θ^- (Assumption 3), and the boundedness of K_r (Remark 1). Specifically, it can be shown by first setting

$$\begin{aligned}&\|\mathbf{W}(t, \mathbf{x}_{p1}, \mathbf{w}_1) - \mathbf{W}(t, \mathbf{x}_{p2}, \mathbf{w}_2)\| \\ &\leq \Big\|\mathbf{W}(t, \mathbf{x}_{p1}, \mathbf{w}_1) - \mathbf{W}(t, \mathbf{x}_{p2}, \mathbf{w}_1)\Big\| + \Big\|\mathbf{W}(t, \mathbf{x}_{p2}, \mathbf{w}_1) - \mathbf{W}(t, \mathbf{x}_{p2}, \mathbf{w}_2)\Big\|.\end{aligned} \tag{A.10}$$

Recalling the definitions of $\mathbf{W}(t, \mathbf{x}_p, \mathbf{w})$ and A in Eqs. (6) and (7), respectively, we have that $A > 0$ (since the kernels K_r and K_θ assume positive values) and thus the first term in Eq. (A.10) reads

$$\begin{aligned}&\|\mathbf{W}(t, \mathbf{x}_{p1}, \mathbf{w}_1) - \mathbf{W}(t, \mathbf{x}_{p2}, \mathbf{w}_1)\| \\ &= \frac{1}{A} \Big\| \int_{\mathcal{S}(\mathbf{x}_{p1})} K_r\left(\|\mathbf{y} - \mathbf{x}_{p1}\|\right) K_\theta \left(\frac{\mathbf{y} - \mathbf{x}_{p1}}{\|\mathbf{y} - \mathbf{x}_{p1}\|} \cdot \frac{\mathbf{w}_1}{\|\mathbf{w}_1\|} \right) \Big(c(t, \mathbf{y}) - c(t, \bar{\mathbf{z}}(\mathbf{x}_{p1}, \mathbf{w}_1)) \Big) \\ &\frac{\mathbf{y} - \mathbf{x}_{p1}}{\|\mathbf{y} - \mathbf{x}_{p1}\|}\, \mathrm{d}\mathbf{y} - \int_{\mathcal{S}(\mathbf{x}_{p2})} K_r\left(\|\mathbf{y} - \mathbf{x}_{p2}\|\right) K_\theta \left(\frac{\mathbf{y} - \mathbf{x}_{p2}}{\|\mathbf{y} - \mathbf{x}_{p2}\|} \cdot \frac{\mathbf{w}_1}{\|\mathbf{w}_1\|} \right) (c(t, \mathbf{y}) \\ &- c(t, \bar{\mathbf{z}}(\mathbf{x}_{p2}, \mathbf{w}_1)))\, \frac{\mathbf{y} - \mathbf{x}_{p2}}{\|\mathbf{y} - \mathbf{x}_{p2}\|}\, \mathrm{d}\mathbf{y} \Big\|.\end{aligned} \tag{A.11}$$

As in [48], exploiting that the direction of polarization $\mathbf{w}_1$ is fixed, proper changes of variables (i.e. $\mathbf{y} = \mathbf{x}_{p1} + \xi$ in the first integral and $\mathbf{y} = \mathbf{x}_{p2} + \xi$ in the second one) allow us to write both integrals on the circular area $\mathcal{S}(\mathbf{0})$ centered at the origin and with radius R. Hence, the boundedness of kernels K_θ and K_r (see Assumption 3 and Remark 1), and the Lipschitz continuity of c

(see Assumption 2), imply the following estimate

$$
\begin{aligned}
\text{(A.11)} &= \frac{1}{A}\Big\| \int_{S(\mathbf{0})} K_r(\|\xi\|)\, K_\theta\left(\frac{\xi}{\|\xi\|}\cdot\frac{\mathbf{w}_1}{\|\mathbf{w}_1\|}\right)\big(c(t,\mathbf{x}_{p1}+\xi) \\
&\quad - c(t,\bar{\mathbf{z}}(\mathbf{x}_{p1},\mathbf{w}_1)) \\
&\quad - c(t,\mathbf{x}_{p2}+\xi) + c(t,\bar{\mathbf{z}}(\mathbf{x}_{p2},\mathbf{w}_1))\big)\frac{\xi}{\|\xi\|}\,\mathrm{d}\xi\Big\| \\
&\le \frac{1}{A}\int_{S(\mathbf{0})} \Big|c(t,\mathbf{x}_{p1}+\xi) - c(t,\mathbf{x}_{p2}+\xi)\Big| \\
&\quad + \Big|c(t,\bar{\mathbf{z}}(\mathbf{x}_{p1},\mathbf{w}_1)) - c(t,\bar{\mathbf{z}}(\mathbf{x}_{p2},\mathbf{w}_1))\Big|\,\mathrm{d}\xi \\
&\le \frac{\pi R^2 \mathrm{Lip}(c)}{A}\Big(\|\mathbf{x}_{p1}-\mathbf{x}_{p2}\| + \|\bar{\mathbf{z}}(\mathbf{x}_{p1},\mathbf{w}_1) - \bar{\mathbf{z}}(\mathbf{x}_{p2},\mathbf{w}_1)\|\Big) \\
&= \underbrace{\frac{2\pi R^2 \mathrm{Lip}(c)}{A}}_{\mathrm{Lip}(\mathbf{W}_\mathbf{x})}\|\mathbf{x}_{p1}-\mathbf{x}_{p2}\|,
\end{aligned}
\tag{A.12}
$$

where the last equality follows from the definition of $\bar{\mathbf{z}}(\mathbf{x}_p,\mathbf{w})$, i.e. $\bar{\mathbf{z}}(\mathbf{x}_p,\mathbf{w}) = \mathbf{x}_p + a\mathbf{w}/\|\mathbf{w}\|R$. Conversely, recalling Eqs. (6), (8), and the boundedness of K_r (see Remark 1), the second term in Eq. (A.10), where cell position $\mathbf{x}_{p2}$ is fixed, reads as follows

$$
\begin{aligned}
&\Big\|\mathbf{W}(t,\mathbf{x}_{p2},\mathbf{w}_1) - \mathbf{W}(t,\mathbf{x}_{p2},\mathbf{w}_2)\Big\| \\
&= \frac{1}{A}\Big\| \int_{S(\mathbf{x}_{p2})} K_r(\|\mathbf{y}-\mathbf{x}_{p2}\|)\, K_\theta\left(\frac{\mathbf{y}-\mathbf{x}_{p2}}{\|\mathbf{y}-\mathbf{x}_{p2}\|}\cdot\frac{\mathbf{w}_1}{\|\mathbf{w}_1\|}\right)(c(t,\mathbf{y}) - c(t,\bar{\mathbf{z}}(\mathbf{x}_{p2},\mathbf{w}_1))) \\
&\quad \frac{\mathbf{y}-\mathbf{x}_{p2}}{\|\mathbf{y}-\mathbf{x}_{p2}\|}\,\mathrm{d}\mathbf{y} - \int_{S(\mathbf{x}_{p2})} K_r(\|\mathbf{y}-\mathbf{x}_{p2}\|)\, K_\theta\left(\frac{\mathbf{y}-\mathbf{x}_{p2}}{\|\mathbf{y}-\mathbf{x}_{p2}\|}\cdot\frac{\mathbf{w}_2}{\|\mathbf{w}_2\|}\right)(c(t,\mathbf{y}) \\
&\quad - c(t,\bar{\mathbf{z}}(\mathbf{x}_{p2},\mathbf{w}_2)))\,\frac{\mathbf{y}-\mathbf{x}_{p2}}{\|\mathbf{y}-\mathbf{x}_{p2}\|}\,\mathrm{d}\mathbf{y}\Big\| \\
&\le \frac{1}{A}\int_{S(\mathbf{x}_{p2})} \Big|K_r(\|\mathbf{y}-\mathbf{x}_{p2}\|)\Big|\Big\|\frac{\mathbf{y}-\mathbf{x}_{p2}}{\|\mathbf{y}-\mathbf{x}_{p2}\|}\Big\|\,\Big|K_\theta\left(\frac{\mathbf{y}-\mathbf{x}_{p2}}{\|\mathbf{y}-\mathbf{x}_{p2}\|}\cdot\frac{\mathbf{w}_1}{\|\mathbf{w}_1\|}\right)(c(t,\mathbf{y}) \\
&\quad - c(t,\bar{\mathbf{z}}(\mathbf{x}_{p2},\mathbf{w}_1))) - K_\theta\left(\frac{\mathbf{y}-\mathbf{x}_{p2}}{\|\mathbf{y}-\mathbf{x}_{p2}\|}\cdot\frac{\mathbf{w}_2}{\|\mathbf{w}_2\|}\right)(c(t,\mathbf{y}) - c(t,\bar{\mathbf{z}}(\mathbf{x}_{p2},\mathbf{w}_2)))\Big|\,\mathrm{d}\mathbf{y}, \\
&\le \frac{1}{A}\int_{S(\mathbf{x}_{p2})} \Big|K_\theta\left(\frac{\mathbf{y}-\mathbf{x}_{p2}}{\|\mathbf{y}-\mathbf{x}_{p2}\|}\cdot\frac{\mathbf{w}_1}{\|\mathbf{w}_1\|}\right)(c(t,\mathbf{y}) - c(t,\bar{\mathbf{z}}(\mathbf{x}_{p2},\mathbf{w}_1))) \\
&\quad - K_\theta\left(\frac{\mathbf{y}-\mathbf{x}_{p2}}{\|\mathbf{y}-\mathbf{x}_{p2}\|}\cdot\frac{\mathbf{w}_2}{\|\mathbf{w}_2\|}\right)(c(t,\mathbf{y}) - c(t,\bar{\mathbf{z}}(\mathbf{x}_{p2},\mathbf{w}_2)))\Big|\,\mathrm{d}\mathbf{y} \\
&\le \frac{1}{A}\left[\int_{S(\mathbf{x}_{p2})} |c(t,\mathbf{y})|\Big|K_\theta\left(\frac{\mathbf{y}-\mathbf{x}_{p2}}{\|\mathbf{y}-\mathbf{x}_{p2}\|}\cdot\frac{\mathbf{w}_1}{\|\mathbf{w}_1\|}\right) - K_\theta\left(\frac{\mathbf{y}-\mathbf{x}_{p2}}{\|\mathbf{y}-\mathbf{x}_{p2}\|}\cdot\frac{\mathbf{w}_2}{\|\mathbf{w}_2\|}\right)\Big|\,\mathrm{d}\mathbf{y}\right. \\
&\quad + \int_{S(\mathbf{x}_{p2})} |c(t,\bar{\mathbf{z}}(\mathbf{x}_{p2},\mathbf{w}_1))|\Big|K_\theta\left(\frac{\mathbf{y}-\mathbf{x}_{p2}}{\|\mathbf{y}-\mathbf{x}_{p2}\|}\cdot\frac{\mathbf{w}_1}{\|\mathbf{w}_1\|}\right) - K_\theta\left(\frac{\mathbf{y}-\mathbf{x}_{p2}}{\|\mathbf{y}-\mathbf{x}_{p2}\|}\cdot\frac{\mathbf{w}_2}{\|\mathbf{w}_2\|}\right)\Big|\,\mathrm{d}\mathbf{y} \\
&\quad \left.+ \int_{S(\mathbf{x}_{p2})} \Big|K_\theta\left(\frac{\mathbf{y}-\mathbf{x}_{p2}}{\|\mathbf{y}-\mathbf{x}_{p2}\|}\cdot\frac{\mathbf{w}_2}{\|\mathbf{w}_2\|}\right)\Big|\,|c(t,\bar{\mathbf{z}}(\mathbf{x}_{p2},\mathbf{w}_1)) - c(t,\bar{\mathbf{z}}(\mathbf{x}_{p2},\mathbf{w}_2))|\,\mathrm{d}\mathbf{y}\right].
\end{aligned}
\tag{A.13}
$$

Thus the boundedness and the Lipschitz continuity of c (see Assumption 2), and the boundedness of K_θ (see Assumption 3) imply that

$$
\begin{aligned}
\text{(A.13)} &\le \frac{2c_0}{A}\int_{S(\mathbf{x}_{p2})} \Big|K_\theta\left(\frac{\mathbf{y}-\mathbf{x}_{p2}}{\|\mathbf{y}-\mathbf{x}_2\|}\cdot\frac{\mathbf{w}_1}{\|\mathbf{w}_1\|}\right) \\
&\quad - K_\theta\left(\frac{\mathbf{y}-\mathbf{x}_{p2}}{\|\mathbf{y}-\mathbf{x}_{p2}\|}\cdot\frac{\mathbf{w}_2}{\|\mathbf{w}_2\|}\right)\Big|\mathrm{d}\mathbf{y} \\
&\quad + \frac{\pi R^2 \mathrm{Lip}(c)}{A}\|\bar{\mathbf{z}}(\mathbf{x}_{p2},\mathbf{w}_1) - \bar{\mathbf{z}}(\mathbf{x}_{p2},\mathbf{w}_2)\| \\
&\le \frac{2c_0}{A}\int_{S(\mathbf{x}_{p2})} \Big|K_\theta\left(\frac{\mathbf{y}-\mathbf{x}_{p2}}{\|\mathbf{y}-\mathbf{x}_{p2}\|}\cdot\frac{\mathbf{w}_1}{\|\mathbf{w}_1\|}\right) - K_\theta\left(\frac{\mathbf{y}-\mathbf{x}_{p2}}{\|\mathbf{y}-\mathbf{x}_{p2}\|}\cdot\frac{\mathbf{w}_2}{\|\mathbf{w}_2\|}\right)\Big|\mathrm{d}\mathbf{y} \\
&\quad + \frac{\pi R^3 |a| \mathrm{Lip}(c) C_{w_0}}{A}\|\mathbf{w}_1 - \mathbf{w}_2\|,
\end{aligned}
\tag{A.14}
$$

where the last inequality follows from the definition of $\bar{\mathbf{z}}(\mathbf{x}_p,\mathbf{w})$ and Proposition 1. Focusing on the last integral in Eq. (A.14), we denote by $U_{\mathbf{x}_p,\mathbf{w}}$ the subset of $\mathcal{S}(\mathbf{x}_p)$ where $K_\theta\left(\frac{\mathbf{y}-\mathbf{x}_p}{\|\mathbf{y}-\mathbf{x}_p\|}\cdot\frac{\mathbf{w}}{\|\mathbf{w}\|}\right) > 0$ and we define three subsets of $\mathcal{S}(\mathbf{x}_{p2})$: $\mathcal{A}_{1,2} := U_{\mathbf{x}_{p2},\mathbf{w}_1} \cap U_{\mathbf{x}_{p2},\mathbf{w}_2}$, $\mathcal{A}_1 := U_{\mathbf{x}_{p2},\mathbf{w}_1} \setminus \mathcal{A}_{1,2}$ and $\mathcal{A}_2 := U_{\mathbf{x}_{p2},\mathbf{w}_2} \setminus \mathcal{A}_{1,2}$ (see the sketch in Fig. A.14 for all possible configurations of $\mathcal{A}_{1,2}$, $\mathcal{A}_1$ and $\mathcal{A}_2$).

The integral in Eq. (A.14) therefore splits as

$$
\begin{aligned}
&\int_{S(\mathbf{x}_{p2})} \Big|K_\theta\left(\frac{\mathbf{y}-\mathbf{x}_{p2}}{\|\mathbf{y}-\mathbf{x}_2\|}\cdot\frac{\mathbf{w}_1}{\|\mathbf{w}_1\|}\right) - K_\theta\left(\frac{\mathbf{y}-\mathbf{x}_{p2}}{\|\mathbf{y}-\mathbf{x}_{p2}\|}\cdot\frac{\mathbf{w}_2}{\|\mathbf{w}_2\|}\right)\Big|\mathrm{d}\mathbf{y} \\
&= \int_{\mathcal{A}_{1,2}} \Big|K_\theta\left(\frac{\mathbf{y}-\mathbf{x}_{p2}}{\|\mathbf{y}-\mathbf{x}_{p2}\|}\cdot\frac{\mathbf{w}_1}{\|\mathbf{w}_1\|}\right) - K_\theta\left(\frac{\mathbf{y}-\mathbf{x}_{p2}}{\|\mathbf{y}-\mathbf{x}_{p2}\|}\cdot\frac{\mathbf{w}_2}{\|\mathbf{w}_2\|}\right)\Big|\mathrm{d}\mathbf{y} \\
&+ \int_{\mathcal{A}_1} \Big|K_\theta\left(\frac{\mathbf{y}-\mathbf{x}_{p2}}{\|\mathbf{y}-\mathbf{x}_{p2}\|}\cdot\frac{\mathbf{w}_1}{\|\mathbf{w}_1\|}\right)\Big|\mathrm{d}\mathbf{y} + \int_{\mathcal{A}_2} \Big|K_\theta\left(\frac{\mathbf{y}-\mathbf{x}_{p2}}{\|\mathbf{y}-\mathbf{x}_{p2}\|}\cdot\frac{\mathbf{w}_2}{\|\mathbf{w}_2\|}\right)\Big|\mathrm{d}\mathbf{y}.
\end{aligned}
\tag{A.15}
$$

It can be then proved that the integrals in the right end term of Eq. (A.15) are bounded by a multiple of $\|\mathbf{w}_1 - \mathbf{w}_2\|$, by using the boundedness of K_θ and (where possible) the Lipschitz continuity of K_θ^+ and K_θ^-, in addition to geometric considerations about the center angle of the circular sectors constituting $\mathcal{A}_{1,2}$, $\mathcal{A}_1$ and $\mathcal{A}_2$. The same result can be proved using instruments of Measure Theory (see for instance [87]). Following the first approach, we can first notice that when the center angle of a circular sector is equal to or lower than the angle between $\mathbf{w}_1$ and $\mathbf{w}_2$, we may take into account that the area of a circular sector spanning between $\mathbf{w}_1$ and $\mathbf{w}_2$ is bounded by $R^2 \|\frac{\mathbf{w}_1}{\|\mathbf{w}_1\|} - \frac{\mathbf{w}_2}{\|\mathbf{w}_2\|}\|$ (see panel (F) in Fig. A.14), and then use Proposition 2. In particular, in the cases shown in panel (A) in Fig. A.14, the Lipschitz continuity of K_θ^+ and K_θ^- allows to estimate the integral on $\mathcal{A}_{1,2}$. Dealing with the integrals on $\mathcal{A}_1$ and $\mathcal{A}_2$, we conversely account for the boundedness of K_θ and observe that the center angles of $\mathcal{A}_1$ and $\mathcal{A}_2$ are equal to the angle between $\mathbf{w}_1$ and $\mathbf{w}_2$. This gives

$$
\text{(A.15)} \le (4\,C_{w_0} + C_\theta \operatorname{acos}\alpha)\,R^2\,\|\mathbf{w}_1 - \mathbf{w}_2\|, \tag{A.16}
$$

where $C_\theta := \mathrm{Lip}(K_\theta^+) + \mathrm{Lip}(K_\theta^-)$.

In the case represented in panel (B) in Fig. A.14, we can use the Lipschitz continuity of K_θ^+ and K_θ^- to estimate only the integral on $\mathcal{A}''_{1,2}$. For other integrals, we apply the boundedness of K_θ and notice that the angle between $\mathbf{w}_1$ and $\mathbf{w}_2$ is larger than the center angles of $\mathcal{A}_1$, $\mathcal{A}_2$ and $\mathcal{A}'_{1,2}$. This way we get

$$
\text{(A.15)} \le (6\,C_{w_0} + C_\theta \operatorname{acos}\alpha)\,R^2\,\|\mathbf{w}_1 - \mathbf{w}_2\|. \tag{A.17}
$$

Conversely, in the cases shown in panel (C) in Fig. A.14, we cannot apply the Lipschitz continuity of K_θ^+ and K_θ^-. However, the angle between $\mathbf{w}_1$ and $\mathbf{w}_2$ is larger than the center angles of $\mathcal{A}_1$, $\mathcal{A}_2$ and $\mathcal{A}'_{1,2}$, and so the boundedness of K_θ leads to

$$
\text{(A.15)} \le 6\,C_{w_0}\,R^2\,\|\mathbf{w}_1 - \mathbf{w}_2\|. \tag{A.18}
$$

If $\mathcal{A}_{1,2}$ is empty (see panel (D) in Fig. A.14), the angle between $\mathbf{w}_1$ and $\mathbf{w}_2$ is larger than both the center angles of $\mathcal{A}_1$ and $\mathcal{A}_2$. Thus the boundedness of K_θ allows us to state that

$$
\text{(A.15)} \le 4\,C_{w_0}\,R^2\,\|\mathbf{w}_1 - \mathbf{w}_2\|. \tag{A.19}
$$

Lastly, if $\mathcal{A}_1$ and $\mathcal{A}_2$ are empty, i.e. if $U_{\mathbf{x}_{p2},\mathbf{w}_1} = U_{\mathbf{x}_{p2},\mathbf{w}_2}$, we have that Eq. (A.15) vanishes if $\mathbf{w}_1 = \mathbf{w}_2$, otherwise (see panel (E) in Fig. A.14) the boundedness of K_θ results in

$$
\text{(A.15)} \le 2\,C_{w_0}\,R^2\,\|\mathbf{w}_1 - \mathbf{w}_2\|, \tag{A.20}
$$

as the center angle of $\mathcal{A}_{1,2}$ is lower than the angle between $\mathbf{w}_1$ and $\mathbf{w}_2$.

Summing up, Eqs. (A.15)–(A.18) give that

$$
\text{(A.15)} \le (6\,C_{w_0} + C_\theta \operatorname{acos}\alpha)\,R^2\,\|\mathbf{w}_1 - \mathbf{w}_2\|, \tag{A.21}
$$

so that Eq. (A.13) reads

$$
\begin{aligned}
&\|\mathbf{W}(t,\mathbf{x}_{p2},\mathbf{w}_1) - \mathbf{W}(t,\mathbf{x}_{p2},\mathbf{w}_2)\| \\
&\le \underbrace{\frac{2c_0 C_{w_0} R^2}{A}\left(6 + \frac{C_\theta}{C_{w_0}}\operatorname{acos}\alpha + \frac{2|a|R}{2c_0}\mathrm{Lip}(c)\right)}_{\mathrm{Lip}(\mathbf{W}_\mathbf{w})}\|\mathbf{w}_1 - \mathbf{w}_2\|,
\end{aligned}
\tag{A.22}
$$

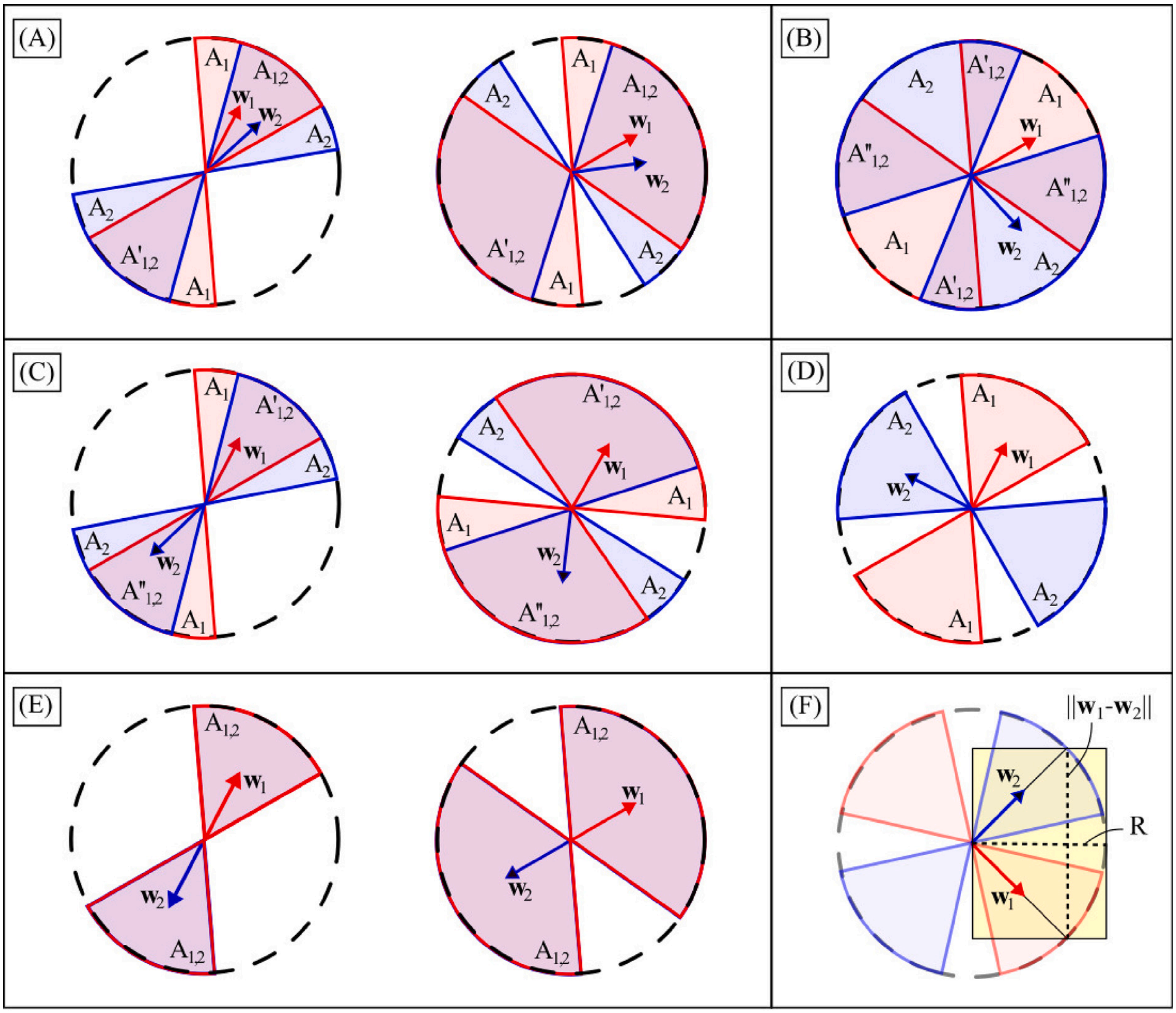

Fig. A.14. Panels (A)-(E): Representation of the circular sectors that form $U_{\mathbf{x}_{p2},\mathbf{w}_1}$ and $U_{\mathbf{x}_{p2},\mathbf{w}_2}$ and their intersection $\mathcal{A}_{1,2} := U_{\mathbf{x}_{p2},\mathbf{w}_1} \cap U_{\mathbf{x}_{p1},\mathbf{w}_2}$ (purple area) for different configurations of $\mathbf{w}_1$ (red arrow) and $\mathbf{w}_2$ (blue arrow) and for different values of α (see Assumption 3). The other circular sectors are $\mathcal{A}_1 := U_{\mathbf{x}_{p2},\mathbf{w}_1} \setminus \mathcal{A}_{1,2}$ (red area) and $\mathcal{A}_2 := U_{\mathbf{x}_{p2},\mathbf{w}_2} \setminus \mathcal{A}_{1,2}$ (blue area). Panel (F): The area of the circular sector spanning from $\mathbf{w}_1$ to $\mathbf{w}_2$ is bounded by the area of the yellow rectangle.

and thus $\mathbf{W}$ results Lipschitz continuous on $\mathcal{X} \times \mathcal{D}$ for any $t \in \mathcal{I}$, since

$$\|\mathbf{W}(t, \mathbf{x}_{p1}, \mathbf{w}_1) - \mathbf{W}(t, \mathbf{x}_{p2}, \mathbf{w}_2)\| \leq \underbrace{\max(\mathrm{Lip}(\mathbf{W}_\mathbf{x}), \mathrm{Lip}(\mathbf{W}_\mathbf{w}))}_{\mathrm{Lip}(\mathbf{W})} \|\mathbf{w}_1 - \mathbf{w}_2\|. \quad \text{(A.23)}$$

Finally, Eq. (A.9) results in

$$\left\| \mathbf{g}_\mathbf{w}(t, \mathbf{x}_{p1}, \mathbf{w}_1) - \mathbf{g}_\mathbf{w}(t, \mathbf{x}_{p2}, \mathbf{w}_2) \right\| \leq \underbrace{\frac{1}{\tau} \max\left\{1, \frac{4 c_0 \pi R^2 + \epsilon}{\epsilon^2} \mathrm{Lip}(\mathbf{W})\right\}}_{\mathrm{Lip}(\mathbf{g}_\mathbf{w})} \Big(\|\mathbf{x}_{p1} - \mathbf{x}_{p2}\| + \|\mathbf{w}_1 - \mathbf{w}_2\| \Big). \quad \text{(A.24)}$$

Eqs. (A.8) and (A.24) then imply the Lipschitz continuity of $\mathbf{F}$ on $\mathcal{X} \times \mathcal{D}$ for any $t \in \mathcal{I}$ and, as already said, Statement 2. ☐

Proof of Statement 3.

Proof. At last, Statement 3 can be proved recalling the formal definition of the solution of the stochastic differential equation (A.2) (see Definition 1), i.e.

$$\mathbf{Z}_1(t) = \mathbf{z}_{0,1} + \int_0^t \mathbf{F}(s, \mathbf{Z}_1(s))\,\mathrm{d}s + \begin{pmatrix} \int_0^t \sqrt{2D}\mathrm{d}\mathbf{B}(s) \\ \mathbf{0} \end{pmatrix}, \quad \text{(A.25)}$$

$$\mathbf{Z}_2(t) = \mathbf{z}_{0,2} + \int_0^t \mathbf{F}(s, \mathbf{Z}_2(s))\,\mathrm{d}s + \begin{pmatrix} \int_0^t \sqrt{2D}\mathrm{d}\mathbf{B}(s) \\ \mathbf{0} \end{pmatrix}, \quad \text{(A.26)}$$

and exploiting the Lipschitz continuity of $\mathbf{F}$ and Gronwall's lemma one can compute for every $t \in \mathcal{I}$

$$\begin{aligned} \|\mathbf{Z}_1(t) - \mathbf{Z}_2(t)\|_{2\times 2} &\leq \|\mathbf{z}_{0,1} - \mathbf{z}_{0,2}\|_{2\times 2} \\ &+ \int_0^t \|\mathbf{F}(s, \mathbf{Z}_1(s)) - \mathbf{F}(s, \mathbf{Z}_2(s))\|_{2\times 2}\,\mathrm{d}s \\ &\leq \|\mathbf{z}_{0,1} - \mathbf{z}_{0,2}\| + \mathrm{Lip}(\mathbf{F}) \int_0^t \|\mathbf{Z}_1(s) - \mathbf{Z}_2(s)\|_{2\times 2}\,\mathrm{d}s \\ &\leq \exp(\mathrm{Lip}(\mathbf{F})\, t)\, \|\mathbf{z}_{0,1} - \mathbf{z}_{0,2}\|_{2\times 2}. \end{aligned} \quad \square \quad \text{(A.27)}$$

Appendix B. Parameters estimation

This Section is devoted to the estimation of the model parameters listed in Table 2. All these values have been used for all the numerical simulations presented in this work. The values of the other parameters are conversely defined in Sections 4.1 and 4.2.

Cell dynamics parameters. The length L of the bidimensional square domain Ω is set equal to 700 μm to reproduce a portion of the substrate used in the biological experiments in [69]. The final time $T = 16$ h has been set to avoid that the cell and its sensing region reach the domain boundaries.

The parameters related to the cell have been set to reproduce the motion of a fibroblast migrating in response to mechanical stimuli, as for example in [15]. The maximal extension of cell protrusions R characterizing the sensing region $\mathcal{S}(\mathbf{x}_p)$ in Eq. (5) is assumed equal to 20 μm in agreement with [48], and with the different values one can find in the biological literature [70].

For what concerns the magnitude of the random motion in Eq. (1), we consider the value of the diffusion coefficient D reported in [71–73] for fibroblasts, i.e. 1.7×10^{-2} μm^2/s.

Referring to Eq. (4), the cell re-orientation time τ is interpreted as the time over which the location of cell lamellipodia changes and, in turn, cell polarization direction varies. Therefore, we set $\tau = 600$ s as reported in [15].

For what concerns the parameter a defining $\bar{\mathbf{z}}(\mathbf{x}_p, \mathbf{w})$ in Eq. (6), in all simulations we assume $a = 0$, noting that the results are not significantly affected by this choice.

The Michaelis–Menten constant ε in Eq. (4) has to be set so that $0 < \varepsilon A \ll 1$, considering that A is defined in Eq. (7) and it depends on the kernels K_r and K_θ.

For the functional form of the kernels defined in Eqs. (9) and (10), the parameters R_0 and α are respectively set equal to 16 μm and $\sqrt{3}/2$ in order to have that the support of kernel K covers 12% of the sensing region, which approximatively corresponds to the area covered by the focal adhesions, as reported in [61,62]. In this case, we obtain $A \approx 314$, and we set $\varepsilon = 0.01/A \approx 3.18 \times 10^{-5}$.

In agreement with [48], the value of V_M in Eq. (2) is set to 0.009 μm/s within the range 0.002–0.012 μm/s estimated in [15] for a fibroblast migrating due to durotaxis. However, we will use the same value also in the case of tensotaxis.

Substrate parameters. When durotaxis is considered, no external loads are applied to the substrate and possible deformations, due to cell–substrate interaction, are assumed so small that the material can be treated as linear elastic whose response is fully characterized by two independent elastic constants, for instance the Poisson ratio, ν, and the Young's modulus, E. In particular, in the present work, we use the Young's modulus, $E(\mathbf{x})$, to quantify stiffness gradients driving cell motion during durotaxis. Specifically, in most of the numerical settings, we will consider Young's modulus varying between 14 and 30 kPa accounting for the measurements reported in [15] regarding a collagen-coated polyacrylamide sheets. In some simulations, the range is increased up to 100 kPa, always staying inside a physiological range [74–76].

Conversely, when tensotaxis is considered, the deformations induced inside the substrate by the external manipulation are not small in general, so that the substrate can be better described by a Yeoh hyperelastic material [49], as discussed in Section 1. About the mechanical properties, the values of the Poisson ratio ν and of the material coefficients μ_1 and μ_3 (that in general can be functions of space) in Eq. (18) are taken from [49], where the substrate is modeled as a polyacrylamide gel (PAG) with different concentrations of acrylamide and bis-acrylamide. Specifically, we set $\nu = 0.48$ due to the quasi-incompressibility of the substrate, whereas the coefficients μ_1 and μ_3 will be defined in Section 4.2, always referring to the ranges reported in [49] (i.e. 1.46–4.66 kPa and 0.25–5.4 kPa, respectively), for the different setups considered in the numerical simulations. We observe that, in the limit of small deformations, the relation $E \approx 4(1+\nu)\mu_1$ holds and the mechanical parameters reported in [49] are in agreement with the ones used in the linear setting by [15].

For what concerns the other parameters defining the mechanical problem given by Eq. (13), the substrate thickness is set as $h = 35$ μm within the range 5–200 μm found in [49].

The constant parameters in Eq. (19) defining the normalization of the energy k_2 and ε_m are respectively set equal to 2 and 5 $(\mathrm{J/m^3})^{1/k_2}$.

Finally, to qualitatively test our model, we consider the surface load given by Eq. (15) defined over a circle $\mathcal{D}$ of radius 23.33 μm placed at the center of the domain Ω then, in Section 4.1, we will consider different values of both the magnitude f_b and direction β of the exerted load.

Appendix C. Supplementary data

Supplementary Materials investigate different functional forms of the kernels and the coupling between ECM density and stiffness.

Supplementary material related to this article can be found online at https://doi.org/10.1016/j.mbs.2023.109124.

References

[1] P. Friedl, D. Gilmour, Collective cell migration in morphogenesis, regeneration and cancer, Nature Rev. Mol. Cell Biol. 10 (7) (2009) 445–457.

[2] E. Sahai, Illuminating the metastatic process, Nat. Rev. Cancer 7 (10) (2007) 737–749.

[3] K. Muraki, K. Tanigaki, Neuronal migration abnormalities and its possible implications for schizophrenia, Front. Neurosci. 9 (2015) 74.

[4] M.B. Prado, M.I. Melo Escobar, R.N. Alves, B.P. Coelho, C.F.L. Fernandes, J.M. Boccacino, R.P. Iglesia, M.H. Lopes, Prion protein at the leading edge: its role in cell motility, Int. J. Mol. Sci. 21 (18) (2020) 6677.

[5] G.S. Rosalem, E.B. Las Casas, T.P. Lima, L.A. González-Torres, A mechanobiological model to study upstream cell migration guided by tensotaxis, Biomech. Model. Mechanobiol. 19 (5) (2020) 1537–1549.

[6] A. Huttenlocher, Cell polarization mechanisms during directed cell migration, Nature Cell Biol. 7 (4) (2005) 336–337.

[7] P. Recho, T. Putelat, L. Truskinovsky, Mechanics of motility initiation and motility arrest in crawling cells, J. Mech. Phys. Solids 84 (2015) 469–505.

[8] D. Ambrosi, A. Zanzottera, Mechanics and polarity in cell motility, Physica D 330 (2016) 58–66.

[9] C. Giverso, L. Preziosi, Mechanical perspective on chemotaxis, Phys. Rev. E 98 (6) (2018) 062402.

[10] J.E. Ron, P. Monzo, N.C. Gauthier, R. Voituriez, N.S. Gov, One-dimensional cell motility patterns, Phys. Rev. Res. 2 (3) (2020) 033237.

[11] P. Maiuri, J. Rupprecht, S. Wieser, V. Ruprecht, O. Bénichou, N. Carpi, M. Coppey, S. De Beco, N. Gov, C. Heisenberg, C. Lage Crespo, F. Lautenschlaeger, M. Le Berre, A. Lennon-Dumenil, M. Raab, H. Thiam, M. Piel, M. Sixt, R. Voituriez, Actin flows mediate a universal coupling between cell speed and cell persistence, Cell 161 (2) (2015) 374–386.

[12] S. SenGupta, C.A. Parent, J.E. Bear, The principles of directed cell migration, Nature Rev. Mol. Cell Biol. 22 (8) (2021) 529–547.

[13] K.J. Painter, Mathematical models for chemotaxis and their applications in self-organisation phenomena, J. Theoret. Biol. 481 (2019) 162–182.

[14] I. Ramis-Conde, M.A.J. Chaplain, A.R.A. Anderson, Mathematical modelling of cancer cell invasion of tissue, Math. Comput. Modelling 47 (5–6) (2008) 533–545.

[15] C.M. Lo, H.B. Wang, M. Dembo, Y.L. Wang, Cell movement is guided by the rigidity of the substrate, Biophys. J. 79 (1) (2000) 144–152.

[16] E.G. Rens, R.M.H. Merks, Cell shape and durotaxis explained from cell-extracellular matrix forces and focal adhesion dynamics, Iscience 23 (9) (2020) 101488.

[17] R. Sunyer, X. Trepat, Durotaxis, Curr. Biol. 30 (9) (2020) R383–R387.

[18] A. Shellard, R. Mayor, Durotaxis: the hard path from in vitro to in vivo, Dev. Cell 56 (2) (2021) 227–239.

[19] B.J. DuChez, A.D. Doyle, E.K. Dimitriadis, K.M. Yamada, Durotaxis by human cancer cells, Biophys. J. 116 (4) (2019) 670–683.

[20] P. Moreo, J.M. García-Aznar, M. Doblaré, Modeling mechanosensing and its effect on the migration and proliferation of adherent cells, Acta Biomater. 4 (3) (2008) 613–621.

[21] K. Schakenraad, L. Ravazzano, N. Sarkar, J.A.J. Wondergem, R.M.H. Merks, L. Giomi, Topotaxis of active brownian particles, Phys. Rev. E 101 (3) (2020) 032602.

[22] N. Ogawa, H. Oku, K. Hashimoto, M. Ishikawa, A physical model for galvanotaxis of paramecium cell, J. Theoret. Biol. 242 (2) (2006) 314–328.

[23] G. Jékely, Evolution of phototaxis, Philos. Trans. R. Soc. B 364 (1531) (2009) 2795–2808.

[24] A. Galante, S. Wisen, D. Bhaya, D. Levy, Stochastic models and simulations of phototaxis, Unifying Themes Complex Syst. 8 (2011) 105–119.

[25] Marcos, H.C. Fu, T.R. Powers, R. Stocker, Bacterial rheotaxis, Proc. Natl. Acad. Sci. 109 (13) (2012) 4780–4785.

[26] K.J. Painter, The impact of rheotaxis and flow on the aggregation of organisms, J. R. Soc. Interface 18 (183) (2021) 20210582.

[27] M.E.M. Stamp, M.S. Brugger, A. Wixforth, C. Westerhausen, Acoustotaxis–in vitro stimulation in a wound healing assay employing surface acoustic waves, Biomater. Sci. 4 (7) (2016) 1092–1099.

[28] A. Veglio, A. Gamba, M. Nicodemi, F. Bussolino, G. Serini, Symmetry breaking mechanism for epithelial cell polarization, Phys. Rev. E 80 (2009) 031919.

[29] C. Wilson, M. Tsuchida, G. Allen, E. Barnhart, K. Applegate, P. Yam, L. Ji, K. Keren, G. Danuser, J. Theriot, Myosin II contributes to cell-scale actin network treadmilling through network disassembly, Nature 465 (7296) (2010) 373–377.

[30] D. Lachowski, E. Cortes, D. Pink, A. Chronopoulos, S.A. Karim, J.P. Morton, A.E.D.R. Hernández, Substrate rigidity controls activation and durotaxis in pancreatic stellate cells, Sci. Rep. 7 (1) (2017) 1–12.

[31] H. Zarkoob, S. Chinnathambi, J.C. Selby, E.A. Sander, Substrate deformations induce directed keratinocyte migration, J. R. Soc. Interface 15 (143) (2018) 20180133.

[32] S.V. Plotnikov, A.M. Pasapera, B. Sabass, C.M. Waterman, Force fluctuations within focal adhesions mediate ECM-rigidity sensing to guide directed cell migration, Cell 151 (7) (2012) 1513–1527.

[33] Z. Sun, S.S. Guo, R. Fässler, Integrin-mediated mechanotransduction, J. Cell Biol. 215 (4) (2016) 445–456.

[34] V. Panzetta, S. Fusco, P.A. Netti, Cell mechanosensing is regulated by substrate strain energy rather than stiffness, Proc. Natl. Acad. Sci. 116 (44) (2019) 22004–22013.

[35] Z. Zhang, P. Rosakis, T.Y. Hou, G. Ravichandran, A minimal mechanosensing model predicts keratocyte evolution on flexible substrates, J. R. Soc. Interface 17 (166) (2020) 20200175.

[36] L.V. Beloussov, N.N. Louchinskaia, A.A. Stein, Tension-dependent collective cell movements in the early gastrula ectoderm of Xenopus laevis embryos, Dev. Genes Evol. 210 (2) (2000) 92–104.

[37] J. Bueno, Y. Bazilevs, R. Juanes, H. Gomez, Droplet motion driven by tensotaxis, Extreme Mech. Lett. 13 (2017) 10–16.

[38] J. Kolega, Effects of mechanical tension on protrusive activity and microfilament and intermediate filament organization in an epidermal epithelium moving in culture, J. Cell Biol. 102 (4) (1986) 1400–1411.

[39] R. Toyoizumi, S. Takeuchi, The behavior of chick gastrula mesodermal cells under the unidirectional tractive force parallel to the substrata, J. Cell Sci. 108 (2) (1995) 557–567.

[40] A. Gagnieu, G. Chagnon, Y. Chemisky, A. Stephanou, A. Chauvière, On the importance of substrate deformations for cell migration, Comput. Methods Biomech. Biomed. Eng. 22 (sup1) (2019) S334–S335.

[41] S. Márquez, G. Reig, M. Concha, R. Soto, Cell migration driven by substrate deformation gradients, Phys. Biol. 16 (6) (2019) 066001.

[42] R. Allena, M. Scianna, L. Preziosi, A cellular potts model of single cell migration in presence of durotaxis, Math. Biosci. 275 (2016) 57–70.

[43] D.K. Schlüter, I. Ramis-Conde, M.A.J. Chaplain, Computational modeling of single-cell migration: the leading role of extracellular matrix fibers, Biophys. J. 103 (6) (2012) 1141–1151.

[44] A. Hassan, T. Biel, T. Kim, Mechanical model for durotactic cell migration, ACS Biomater. Sci. Eng. 5 (8) (2019) 3954–3963.

[45] A.A. Malik, P. Gerlee, Mathematical modelling of cell migration: stiffness dependent jump rates result in durotaxis, J. Math. Biol. 78 (7) (2019) 2289–2315.

[46] G. Yu, J. Feng, H. Man, H. Levine, Phenomenological modeling of durotaxis, Phys. Rev. E 96 (1) (2017) 010402.

[47] G. De Santis, A.B. Lennon, F. Boschetti, B. Verhegghe, P. Verdonck, P.J. Prendergast, How can cells sense the elasticity of a substrate? An analysis using a cell tensegrity model, Eur. Cells Mater. 22 (2011) 202–213.

[48] A. Colombi, S. Falletta, M. Scianna, L. Scuderi, An integro-differential non-local model for cell migration and its efficient numerical solution, Math. Comput. Simulation 180 (2021) 179–204.

[49] T. Boudou, J. Ohayon, C. Picart, R.I. Pettigrew, P. Tracqui, Nonlinear elastic properties of polyacrylamide gels: implications for quantification of cellular forces, Biorheology 46 (3) (2009) 191–205.

[50] C. Mezzacappa, Y. Komiya, R. Habas, Activation and function of small GTPases Rho, RAC, and CDC42 during gastrulation, in: K. Turksen (Ed.), Planar Cell Polarity. Methods in Molecular Biology, Vol. 839, Springer, New York, 2012, pp. 266–290.

[51] J.A. Espina, C.L. Marchant, E.H. Barriga, Durotaxis: the mechanical control of directed cell migration, FEBS J. 289 (10) (2022) 2736–2754.

[52] S. Li, P. Butler, Y. Wang, Y. Hu, D.C. Han, S. Usami, J. Guan, S. Chien, The role of the dynamics of focal adhesion kinase in the mechanotaxis of endothelial cells, Proc. Natl. Acad. Sci. USA 99 (2002) 3546–3551.

[53] B. Øksendal, Stochastic Differential Equations: An Introduction with Applications, Springer Science & Business Media, 2013.

[54] R. Durrett, Brownian Motion, 5 edition, in: Cambridge Series in Statistical and Probabilistic Mathematics, Cambridge University Press, 2019, pp. 305–335.

[55] L.C.G. Rogers, D. Williams, Diffusions, Markov Processes and Martingales, 2 edition, in: Cambridge Mathematical Library, vol. 2, Cambridge University Press, 2000.

[56] H. Risken, The Fokker–Planck equation: Methods of Solution and Applications, Springer, 1996.

[57] C. Giverso, N. Loy, G. Lucci, L. Preziosi, Cell orientation under stretch: A review of experimental findings and mathematical modelling, J. Theoret. Biol. 572 (2023) 111564.

[58] C.A. Parent, P.N. Devreotes, A cell's sense of direction, Science 284 (5415) (1999) 765–770.

[59] C.A. Parent, B.J. Blacklock, W.M. Froehlich, D.B. Murphy, P.N. Devreotes, G protein signaling events are activated at the leading edge of chemotactic cells, Cell 95 (1) (1998) 81–91.

[60] A. Hunter, C.W. Archer, P.S. Walker, G.W. Blunn, Attachment and proliferation of osteoblasts and fibroblasts on biomaterials for orthopaedic use, Biomaterials 16 (4) (1995) 287–295.

[61] M. Prager-Khoutorsky, A. Lichtenstein, R. Krishnan, K. Rajendran, A. Mayo, Z. Kam, B. Geiger, A.D. Bershadsky, Fibroblast polarization is a matrix-rigidity-dependent process controlled by focal adhesion mechanosensing, Nature Cell Biol. 13 (12) (2011) 1457–1465.

[62] S. Ryoo, Y. Kim, M. Kim, D. Min, Behaviors of NIH-3T3 fibroblasts on graphene/carbon nanotubes: proliferation, focal adhesion, and gene transfection studies, ACS Nano 4 (11) (2010) 6587–6598.

[63] U. Horzum, B. Ozdil, D. Pesen-Okvur, Step-by-step quantitative analysis of focal adhesions, MethodsX 1 (2014) 56–59.

[64] E. Ruoslahti, RGD and other recognition sequences for integrins, Annu. Rev. Cell Dev. Biol. 12 (1) (1996) 697–715.

[65] C. Gaudet, W.A. Marganski, S. Kim, C.T. Brown, V. Gunderia, M. Dembo, J.Y. Wong, Influence of type I collagen surface density on fibroblast spreading, motility, and contractility, Biophys. J. 85 (5) (2003) 3329–3335.

[66] H.E. Balcioglu, L. Balasubramaniam, T.V. Stirbat, B.L. Doss, M. Fardin, R. Mège, B. Ladoux, A subtle relationship between substrate stiffness and collective migration of cell clusters, Soft Matter 16 (7) (2020) 1825–1839.

[67] E.A. Cavalcanti-Adam, T. Volberg, A. Micoulet, H. Kessler, B. Geiger, J.P. Spatz, Cell spreading and focal adhesion dynamics are regulated by spacing of integrin ligands, Biophys. J. 92 (8) (2007) 2964–2974.

[68] T. Sauer, Numerical solution of stochastic differential equations in finance, in: Handbook of Computational Finance, Springer, 2012, pp. 529–550.

[69] E. Theveneau, B. Steventon, E. Scarpa, S. Garcia, X. Trepat, A. Streit, R. Mayor, Chase-and-run between adjacent cell populations promotes directional collective migration, Nature Cell Biol. 15 (7) (2013) 763–772.

[70] B. Alberts, A. Johnson, J. Lewis, M. Raff, K. Roberts, P. Walter, Molecular Biology of the Cell, 4th edition, Garland Science, New York, 2002.

[71] L. Olsen, J.A. Sherratt, P.K. Maini, A mechanochemical model for adult dermal wound contraction and the permanence of the contracted tissue displacement profile, J. Theoret. Biol. 177 (2) (1995) 113–128.

[72] Y. Kim, J. Wallace, F. Li, M. Ostrowski, A. Friedman, Transformed epithelial cells and fibroblasts/myofibroblasts interaction in breast tumor: A mathematical model and experiments, J. Math. Biol. 61 (3) (2010) 401–421.

[73] A. Häcker, A mathematical model for mesenchymal and chemosensitive cell dynamics, J. Math. Biol. 64 (1) (2012) 361–401.

[74] Y. Yang, K. Xie, H. Jiang, Durotaxis index of 3t3 fibroblast cells scales with stiff-to-soft membrane tension polarity, Biophys. J. 119 (7) (2020) 1427–1438.

[75] Y. Yu, L. Ren, X. Liu, X. Gong, W. Yao, Effects of substrate stiffness on mast cell migration, Eur. J. Cell Biol. 100 (7–8) (2021) 151178.

[76] R. Sunyer, A.J. Jin, R. Nossal, D.L. Sackett, Fabrication of hydrogels with steep stiffness gradients for studying cell mechanical response, PLoS One 7 (10) (2012) e46107.

[77] E. Agliari, E. Biselli, A. De Ninno, G. Schiavoni, L. Gabriele, A. Gerardino, F. Mattei, A. Barra, L. Businaro, Cancer-driven dynamics of immune cells in a microfluidic environment, Sci. Rep. 4 (6639) (2014).

[78] L.G. Vincent, Y.S. Choi, B. Alonso-Latorre, J.C. del Álamo, A.J. Engler, Mesenchymal stem cell durotaxis depends on substrate stiffness gradient strength, Biotechnol. J. 8 (4) (2013) 472–484.

[79] I.V. Dokukina, M.E. Gracheva, A model of fibroblast motility on substrates with different rigidities, Biophys. J. 98 (12) (2010) 2794–2803.

[80] D. Ambrosi, Cellular traction as an inverse problem, SIAM J. Appl. Math. 66 (6) (2006) 2049–2060.

[81] R. Merkel, N. Kirchgeßner, C.M. Cesa, B. Hoffmann, Cell force microscopy on elastic layers of finite thickness, Biophys. J. 93 (9) (2007) 3314–3323.

[82] R. Sopher, H. Tokash, S. Natan, M. Sharabi, O. Shelah, O. Tchaicheeyan, A. Lesman, Nonlinear elasticity of the ECM fibers facilitates efficient intercellular communication, Biophys. J. 115 (7) (2018) 1357–1370.

[83] S. Goren, M. Levin, G. Brand, A. Lesman, R. Sorkin, Probing local force propagation in tensed fibrous gels, Small 19 (4) (2023) 2202573.

[84] G. Reig, M. Cerda, N. Sepúlveda, D. Flores, V. Castañeda, M. Tada, S. Härtel, M.L. Concha, Extra-embryonic tissue spreading directs early embryo morphogenesis in killifish, Nature Commun. 8 (1) (2017) 15431.

[85] E.H. Barriga, E. Theveneau, In vivo neural crest cell migration is controlled by mixotaxis, Front. Physiol. 11 (2020) 586432.

[86] D. Baruffaldi, G. Palmara, C. Pirri, F. Frascella, 3D cell culture: recent development in materials with tunable stiffness, ACS Appl. Bio Mater. 4 (3) (2021) 2233–2250.

[87] V.I. Bogachev, M.A.S. Ruas, Measure Theory, Vol. 1, Springer, 2007.